Research Article **AJGRR (2017) 1:3**

American Journal of Geographical Research and Reviews
(ISSN:2577-4433)

From Micro- to Satellite Gravity: Understanding the Earth

Lev V. Eppelbaum

School of Geosciences, Faculty of Exact Sciences, Tel Aviv University, Ramat Aviv 6997801, Tel Aviv, Israel

ABSTRACT

The main physical principle of gravity method application is the difference in densities between the various geological, environmental, archaeological and other targets and host media. Gravity is one of the oldest geophysical methods and it is widely applied for knowledge of subsurface and deep Earth's domains. The present review displays multiscale examples of gravity field examination: from very detailed (delineation of karst terranes and archaeological targets) to regional investigations (development of 3D physical-geological models and satellite data examination of giant regions). Geographically the examined areas include the South Caucasus, the Dead Sea region, the Eastern Mediterranean and the Arabian-African region. Diverse methodologies of the gravity data processing, qualitative and quantitative interpretation, and results of 3D gravity field modeling are shown. It is demonstrated that integration of gravity field analysis with other geophysical methods (magnetic, paleomagnetic, thermal, seismic, etc.) significantly increases accuracy and reliability of developed physical-geological models. The further ways of evaluation of gravity data analysis are considered.

Keywords: gravity noise, gravity field transformations, quantitative analysis, 3D gravity models, South Caucasus, Eastern Mediterranean, Arabian-African region, subsurface targets, regional reconstructions

***Correspondence to Author:**
Lev V. Eppelbaum
School of Geosciences, Faculty of Exact Sciences, Tel Aviv University, Ramat Aviv 6997801, Tel Aviv, Israel

How to cite this article:
Lev V. Eppelbaum. From Micro- to Satellite Gravity: Understanding the Earth. American Journal of Geographical Research and Reviews, 2017; 1:3.

eSciencePublisher
eSciPub LLC, Houston, TX USA.
Website: http://escipub.com/

1. Introduction

It is known that four physical forces control the Universe [1]. Gravity is most obvious and seems to be simplest from these forces. However, it is only apparent simplicity since the gravity field analysis in complex media is not a trivial task. Gravity as a physical effect plays a huge role both on its own and other laws and peculiarities. All the people lives (together with fauna and flora), different tectonic-geodynamic and meteorological processes and events, go on the gravitating rotating inhomogeneous ellipsoid, on which (besides all) influence other cosmic bodies.

Comprehensive analysis carried out by Aleinikov et al. [2] indicates that even analyzing a simple case of gravitating rotating sphere consisting of the homogeneous hard envelope and liquid core, the physical-mathematical examination of stresses and deformations in the Earth is sufficiently complex. These difficulties are dramatically increase by transfer to the real inhomogeneous ellipsoid consisting of numerous geological-geophysical boundaries and slabs.

Development of the modern generation of surface field gravimetric equipment enables the explorer to register measurements promptly in 1 microGal (10^{-8} m/s^2) and tenths of Eötvös (1E = 10^{-9} 1/s^2). It opens up new opportunities for solving earlier unacceptable problems in the gravity field analysis. Satellite gravity measurements covered almost all the Earth, and accuracy of the data retracked to the marine and land surfaces is about 1 mGal (10^{-5} m/s^2) [e.g., 3-5].

The conventional gravity data processing and reductions are presented in detail in many books [e.g., 6-15]. Thus, the author preferred to concentrate on the gravity method application to solve various geological-geophysical problems, mainly using his own experience.

The size of the paper does not allow to display all the variety of gravity field examinations. Therefore, here shown only some characteristic examples of gravity studies in environmental and archaeological geophysics, localization of economic deposits, regional geophysical investigations and satellite gravity examination. Nevertheless, the author hopes that the presented examples accompanied by some brief reviews clearly show significance of the gravity data analysis in understanding the Earth' structure and its subsurface/environment.

The examples shown in the paper evidently indicate that in complex geological situations combining gravity field analysis with other geophysical methods (magnetic, paleomagnetic, thermal, seismic, etc.) sharply increases interpretation reliability and accuracy.

2. Different Kinds of Noise in Gravity Field Examination

A gravity survey is the geophysical method most affected by different kinds of noise (disturbances). A chart showing the different types of typical noise factors is presented in Figure 1 (after [16]). These types of noise are described in more detail below.

Artificial (man-made) noise. The *industrial* component of noise mostly comes from surface and underground engineering constructions, transportation and communications lines, garbage dumps, etc. The *instrumental* component is associated with the physical-technical properties of gravimeters (e.g., shift zero) and gradiometers. *Human errors* of different kinds, obviously, will accompany geophysical observations at any time. Finally, *undocumented* (*poorly documented*) results of previous surveys can misrepresent preliminary Physical-Geological Models (*PGM*) development.

Natural disturbances. *Nonstationary* noise includes, for instance, known tidal effects. *Meteorological conditions* (temperature, rain, lightning, snow, hurricanes, etc.) can also affect gravimeter readings. Corrections for the *atmosphere* deserve special attention in microgravity investigations, since the air layer

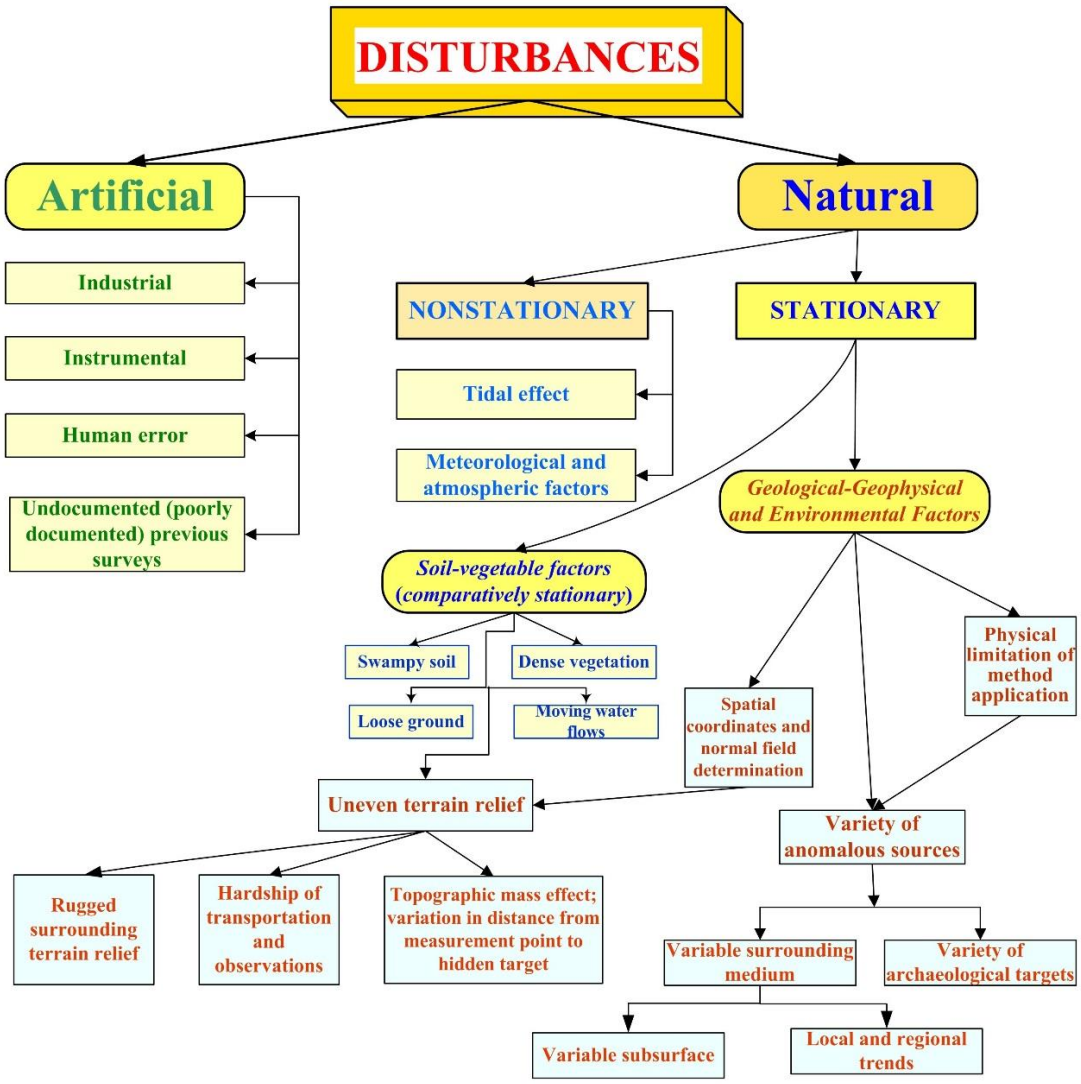

Figure 1. A generalized block-scheme of noise in gravity investigations (modified after [16]).

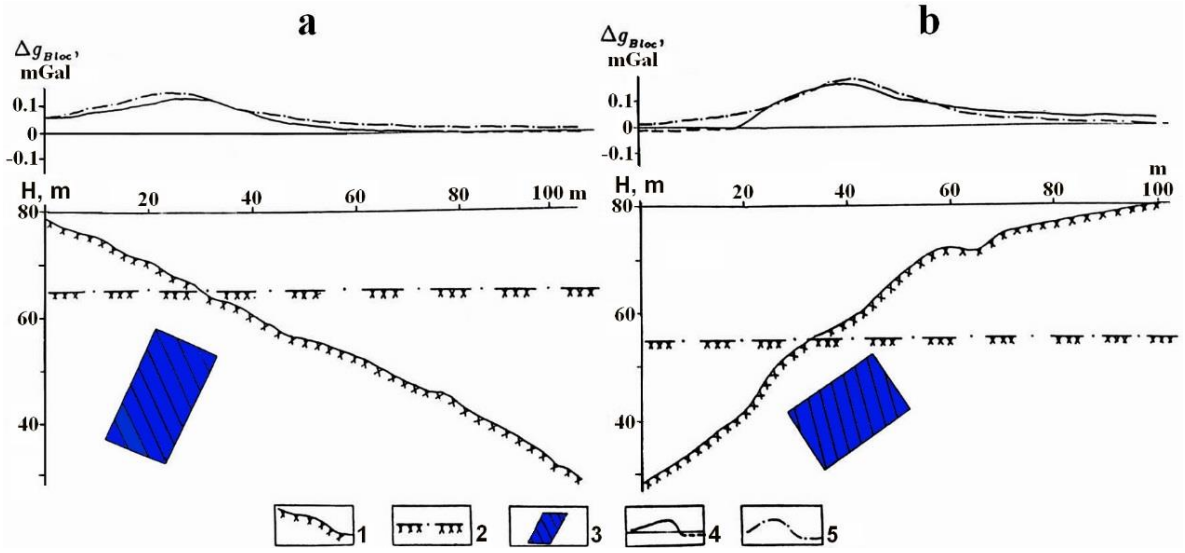

Figure 2. Negative effect of gravitational anomalies from a local anomalous body observed on inclined and horizontal profiles (after [11], with significant modifications. (a) smooth slope, (b) complicated slope. (1) Profile flowing the relief points; (2) horizontal profile; (3) anomalous body with a positive contrast density $\Delta\sigma$ = 1500 kg/m^3; anomaly Δg_B after the topographic mass attraction correction: (4) along profile (1), (5) along profile (2).

attraction is different at various levels over and below the m.s.l. *Soil-vegetation factors* associated with certain soil types (e.g., swampy soil or loose ground in deserts and in some other areas) and dense vegetation, which may hamper movement along the profile, also need to be taken into account.

Geological-geophysical and environmental factors. This group presents the most significant physical-geological disturbances. The application of gravity method depends primarily on the existence of density contrast between the objects under study and the surrounding medium.

The *physical limitation of method application* assesses the measurable density contrast properties between the anomalous targets and the host media, as well as corresponding size of targets and depths of their occurring.

Spatial coordinates and normal gravity field determination are also vital to gravity field analysis and any inaccuracies here may cause significant errors in subsequent analyses.

Uneven terrain relief can impede the observer's movement and restrict gravity data acquisition. Physically, this kind of gravity noise is affected by the form and density of the topographic features composing the relief, as well as *variations in the distance from the point of measurement to the hidden target* [11]. Calculations of the effects from the *surrounding terrain relief* (sometimes for radii up to 200 km) are also of great importance [10,17].

The *variety of anomalous sources* is composed of two factors: *the variable surrounding medium* and *the variety of anomalous targets*. Both these factors are crucial and greatly complicate the interpretation of magnetic data.

Variable subsurface can make it difficult to determine the correct densities of bodies occurring close to the earth's surface.

Local and regional trends (linear, parabolic or other types) often mask the target gravity effects considerably [e.g., 7,10,11,17]. Sometimes regional gravity trend effects may exceed local desired anomalies by some tenfold.

Let us consider the last disturbing factor in detail. The correct removal (elimination) of regional trends is not a trivial task [e.g., 10,13]. Figure 2 shows two cases of non-horizontal gravity observations with the presence of an anomalous body occurring closely to the earth's surface. For a 3D gravity field computation (here and in other presented gravity field computations) a developed *GSFC* (Geological Space Field Computation) software was employed. The basic algorithm realized in the *GSFC* program is the solution of the direct 3-D problem of gravity and magnetic fields for the horizontal polygonal prism by limited in the strike direction [18].

The distorting effect of a non-horizontal observation line occurs when the anomalous target differs from the surrounding medium by density that produces an anomalous vertical gradient. Analysis of the Δg_B anomalies observed on the horizontal and inclined rugged relief indicates that the gravity effects in these situations are cardinal different (Figure 2). Despite the fact that the free air and Bouguer reductions were applied to the observations on the inclined relief, the computed Bouguer anomaly is characterized by small negative values (minimum) in the downward direction of the relief, whereas the anomaly on the horizontal profile has no negative values. Theoretically it is not possible since the gravity effect from body with a positive contrast density (1500 kg/m^3) occurring in the homogenous medium must be only positive and tends to zero at far distances from the target.

Thus, applying the conventional corrections does not eliminate this trend because the observation points for the anomalous object are significantly different and the large anomalous body occurs closely to the observation points [11]. Hence, a special methodology is required for gravimetric quantitative anomaly interpretation in the conditions of rugged relief [16].

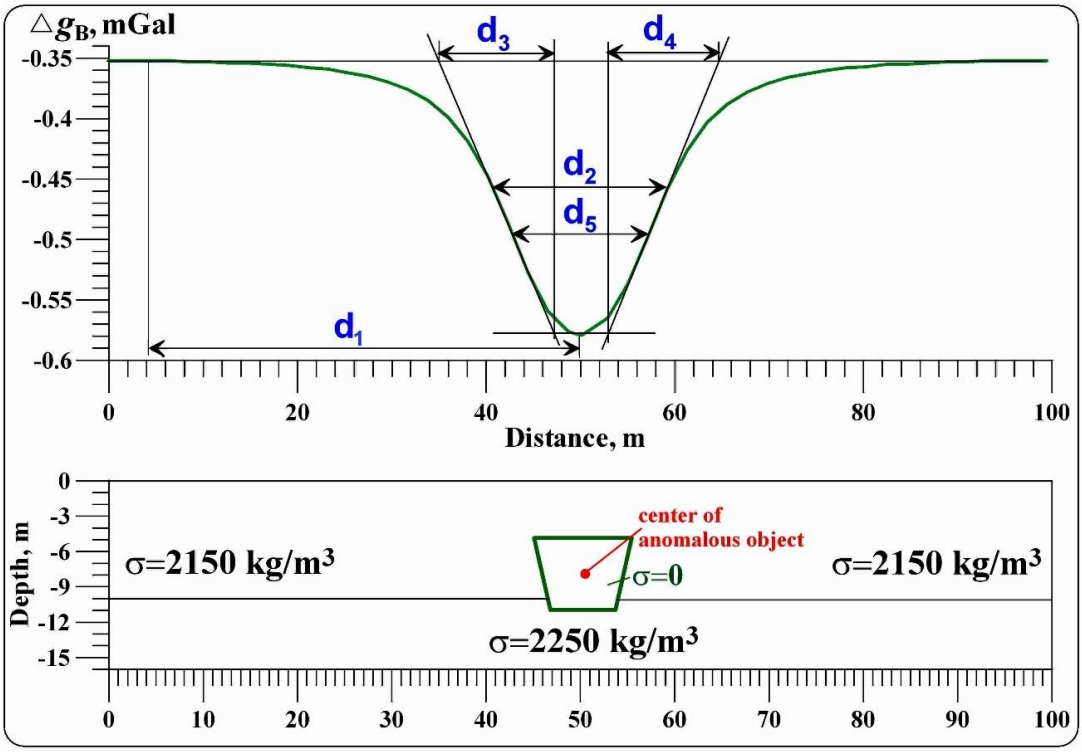

Figure 3. Quantitative analysis of gravity anomaly by the use of advanced methods developed in magnetic prospecting

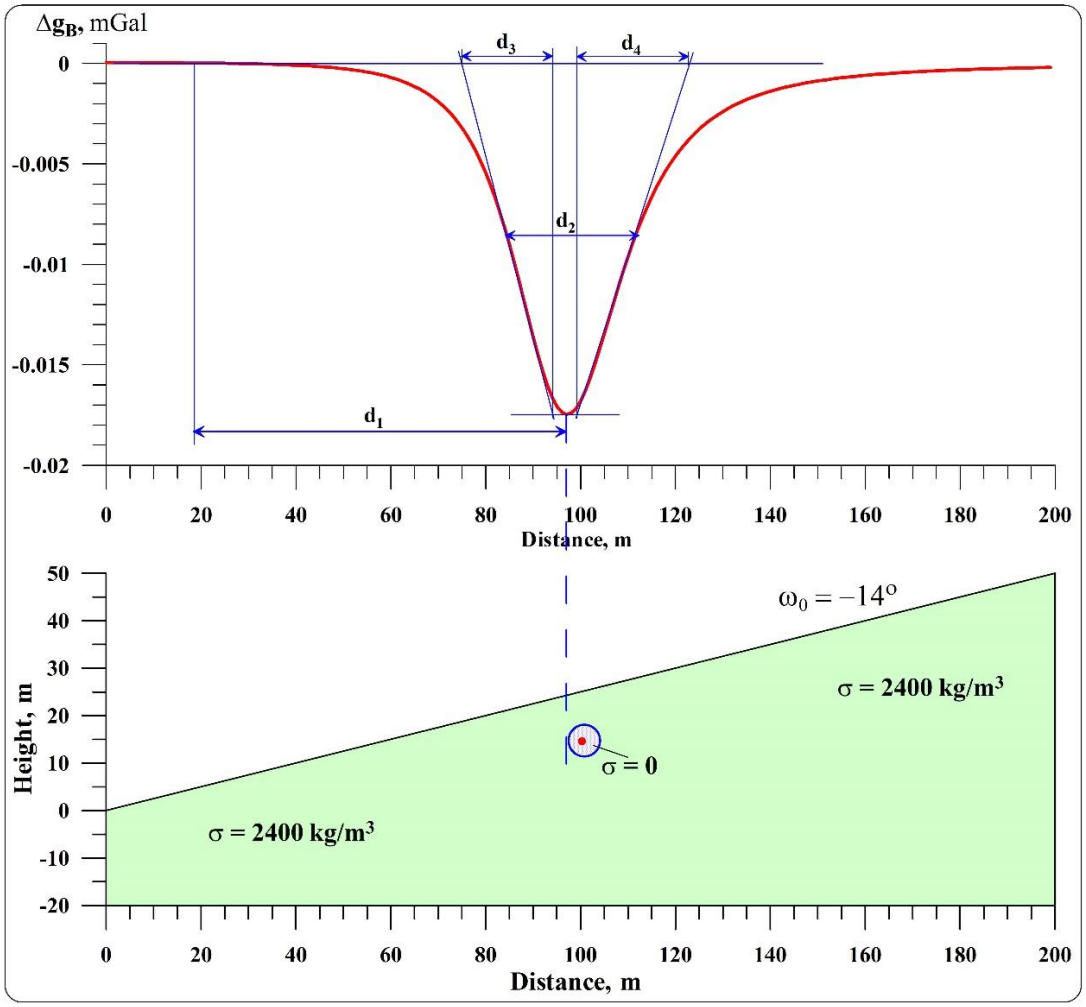

Figure 4. Quantitative analysis of gravity anomaly on inclined profile from a buried sphere

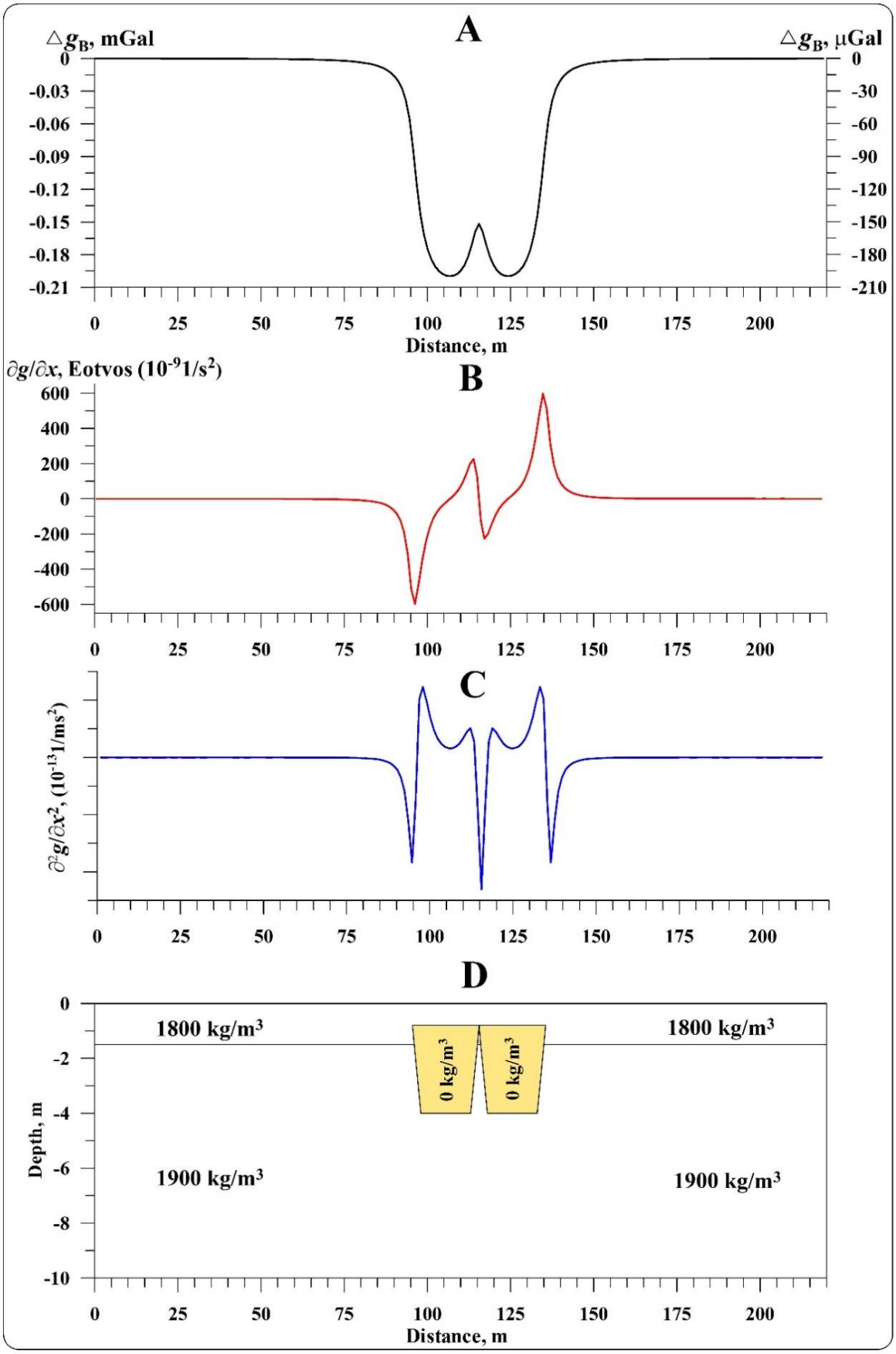

Figure 5. Computing of horizontal derivatives of gravity field for the models of closely located karst bodies. **(A)** Computed gravity curve (level of computation: 0.3 m), **(B)** Calculated first horizontal derivative of gravity field Δg_x, **(C)** Calculated second horizontal derivative Δg_{xx}, **(D)** Physical-geological model (after [24], with modifications)

3. Quantitative analysis of gravity anomalies

It is known that conventional methods of gravity anomaly quantitative analysis, utilizing amplitude changing at definite distances from the anomaly center [e.g., 10], are correct only in simplest situations.

The gravity field intensity **F** is expressed as [e.g., 12]:

$$\mathbf{F} = -grad\, W, \qquad (1)$$

where *W* is the gravity potential.

For an anomalous magnetic field $\mathbf{U_a}$ one can write (when the magnetic susceptibility is ≤ 0.1 SI units) [11]:

$$\mathbf{U_a} = -grad\, V, \qquad (2)$$

where *V* represents the magnetic potential.

Let us consider analytical expressions of some typical models employed in magnetic and gravity fields (Table 1).

Table 1. Comparison of some analytical expressions for magnetic and gravity fields

Field	Analytical expression	
Magnetic	Thin bed (TB) $Z_v = 2I2b\frac{z}{z^2+z^2}$ (3)	Point source (rod) $Z_v = \frac{mz}{\left(z^2+z^2\right)^{3/2}}$ (4)
Gravity	Horizontal Circular Cylinder (HCC) $\Delta g = 2G\sigma\frac{z}{z^2+z^2}$ (5)	Sphere $\Delta g = GM\frac{z}{\left(z^2+z^2\right)^{3/2}}$ (6)

Here Z_v is the vertical magnetic field component at vertical magnetization, *I* is the magnetization, *b* is the horizontal semi-thickness of TB, *m* is the elementary magnetic mass, *z* is the depth to the center of the body (for HCC and sphere) and the depth to the upper edge of TB and rod (point source), and *M* is the mass of the sphere.

It is clear that expressions (1) and (2) are analogical and equations (3) and (5), (4) and (6), respectively, are proportional.

Thus, we can apply the advanced interpreting methodologies developed in magnetic prospecting for complex environments [11,16] to gravity field analysis. For instance, we can interpret anomalies from the gravity HCC by formulas employed in the magnetic TB (improved tangent, characteristic point and areal methods).

We can also calculate the "gravity moment" (analogically to "magnetic moment" used in magnetic field examination), which can be used for classification and ranking of gravity anomalies produced by various kinds of targets. For example, the "gravity moment" of horizontal circular cylinder (HCC) can be calculated by the use of the corresponding equation for the magnetic thin bed (TB) [16]:

$$M_{\Delta g} = \tfrac{1}{2}\Delta g_a h, \qquad (7)$$

where $M_{\Delta g}$ is the gravity moment, Δg_a is the amplitude of the gravity anomaly (in mGal) and *h* is the depth of the HCC occurrence (in meters).

A significant number of field areas are located in conditions of rugged terrain relief. Uneven observation profiles (or areas) are responsible for variations in the distance from the points of measurement to the anomalous target and can impede quantitative examination of gravity anomalies [16]. If anomalies observed on an inclined profile, the obtained parameters characterize a certain fictitious body. Calculating real body parameters from fictitious body parameters can be done by applying the

following expressions (the subscript "*r*" stands for a parameter of the real body):

$$\left.\begin{aligned} h_r &= h + x \cdot \tan\omega_0 \\ x_r &= -h \cdot \tan\omega_0 + x \end{aligned}\right\}, \qquad (8)$$

where h is the depth of the upper edge occurrence, x_0 is the location of the source's projection to plan relative to the extremum having the greatest magnitude, and ω_0 is the angle of the terrain relief inclination ($\omega_0 > 0$ when the inclination is toward the positive direction of the x-axis).

A model of karst cavity presented in Figure 3 occurs at the boundary of two layers with different densities. Quantitative examination of this anomaly by the use of conventional method [e.g., 7] leads to large mistakes. At the same time, employment of quantitative interpretation methods developed in magnetic prospecting (improved modifications of tangents, characteristic points and areal method) [e.g., 19,20] enabled to determine a center of this anomalous body with high accuracy (Figure 3). Calculated $M_{\Delta g}$ in this example is

$$\tfrac{1}{2} \cdot 7\,\text{m} \cdot 0.23\,\text{mGal} \cong 0.805\,\text{mGal} \cdot \text{m}.$$

An example of interpreting a gravity anomaly from a buried cavity on an inclined profile is presented in Figure 4. It should be noted that if the borehole is drilled on the projection of the gravity anomaly minimum to the earth's surface, the borehole which will be drilled at this point would not localize the target (due to the disturbing effect of the inclined relief).

Application of the improved modification of tangent method [16] together with Eq. (8) was used to obtain the position of the cavity center (bold red point in Figure 4) with sufficient accuracy. $M_{\Delta g}$ in this example consists of

$$\tfrac{1}{2} \cdot 10.5\,\text{m} \cdot 0.0175\,\text{mGal} \cong 0.092\,\text{mGal} \cdot \text{m}.$$

4. Some Implementations of Gravity Field Analysis

4.1. Geological-geophysical mapping

As a rule, gravity method is a necessary component of geological-geophysical mapping of different scales [e.g., 7,10,11, 15-17]. Delineation of faults is one of the most important tasks of the mapping. The main geological-geophysical indicators of various faults reflected in gravity and magnetic fields are summarized in Table 2.

Table 2. Gravity and magnetic fields over faults (after [17], with modifications)

Types of fractures	Geological characteristics	Reflections in fields
Faults – channels for magma flows	Fractured zones filled with basic rocks Intrusions or volcanic centers localized along fractured zone	Linearly elongated positive anomalies Chain of near-isometric maxima, or sometimes minima
Contemporaneous (growth) faults	Abrupt changes in lithological composition, facies and deposit thickness on both sides of a fault	Change of sign or behavior of the same sign field at the fault
Faults fixing vertical displacement of geological blocks	Abrupt changes of boundary positions separating a section into individual structural facial complexes Crush zone due to differentiated movement of conjugated blocks along the fault	Zone of high field gradients (an additional criterion is an abrupt change in occurrence depth for upper or lower anomalous mass edges) Chain of linearly elongated magnetic and gravity minima coincident in plan
Faults fixing horizontal displacement of geological blocks	Horizontal rock displacement determined by comparing age, structural and facies features of rocks on both sides of a fault	Rupture and echelon displacement of zones with linearly elongated anomalies, abruptly inflected isolines

4.2. Environment

4.2.1. Karst terranes

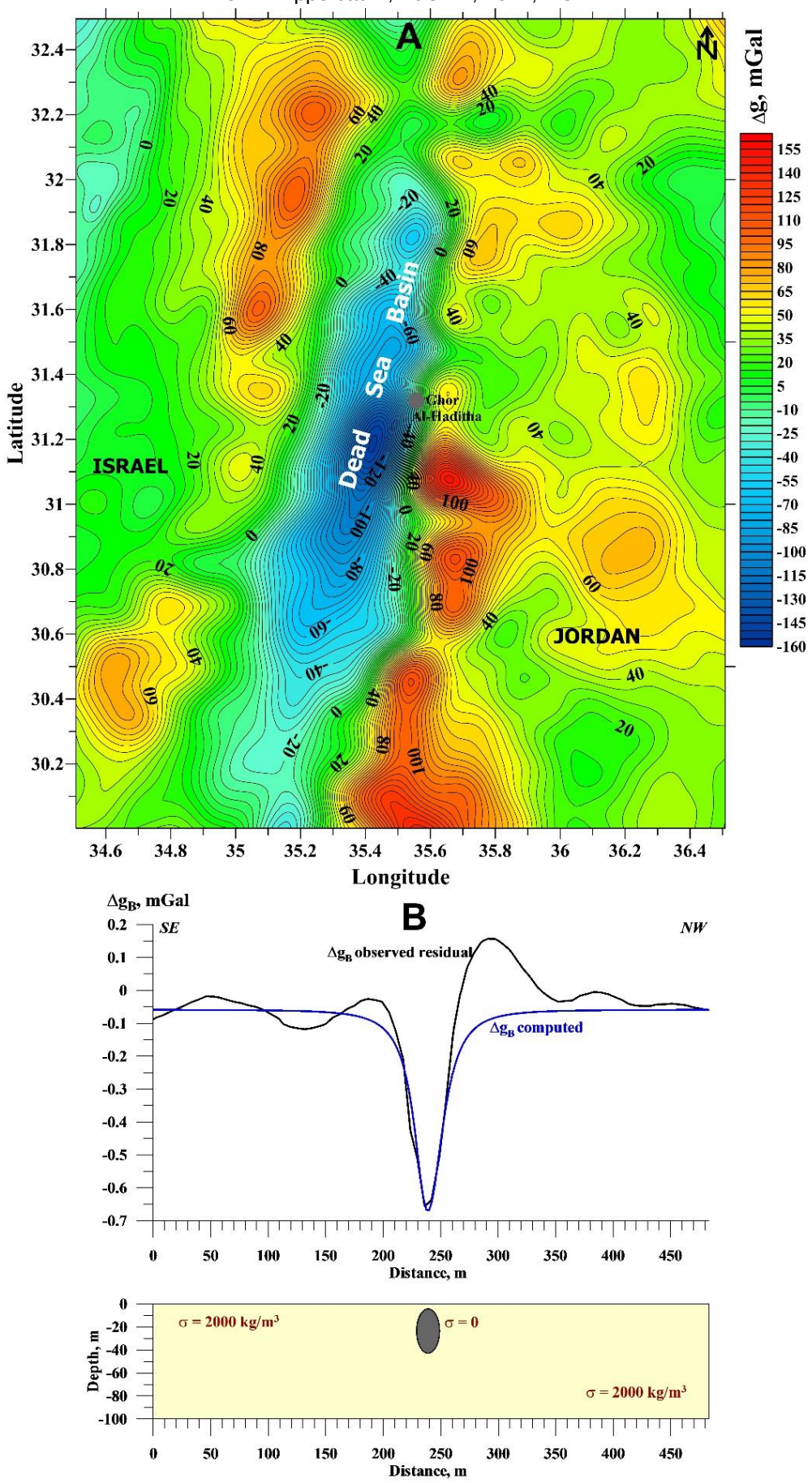

Figure 6. **A**. Satellite derived gravity map with location of the Ghor Al-Haditha site (eastern coast of the Dead Sea, Jordan). **B**. An initial physical-geological model along the profile in this site, developed on the basis of 3D gravity field modeling (surface data) (after [26], with modifications).

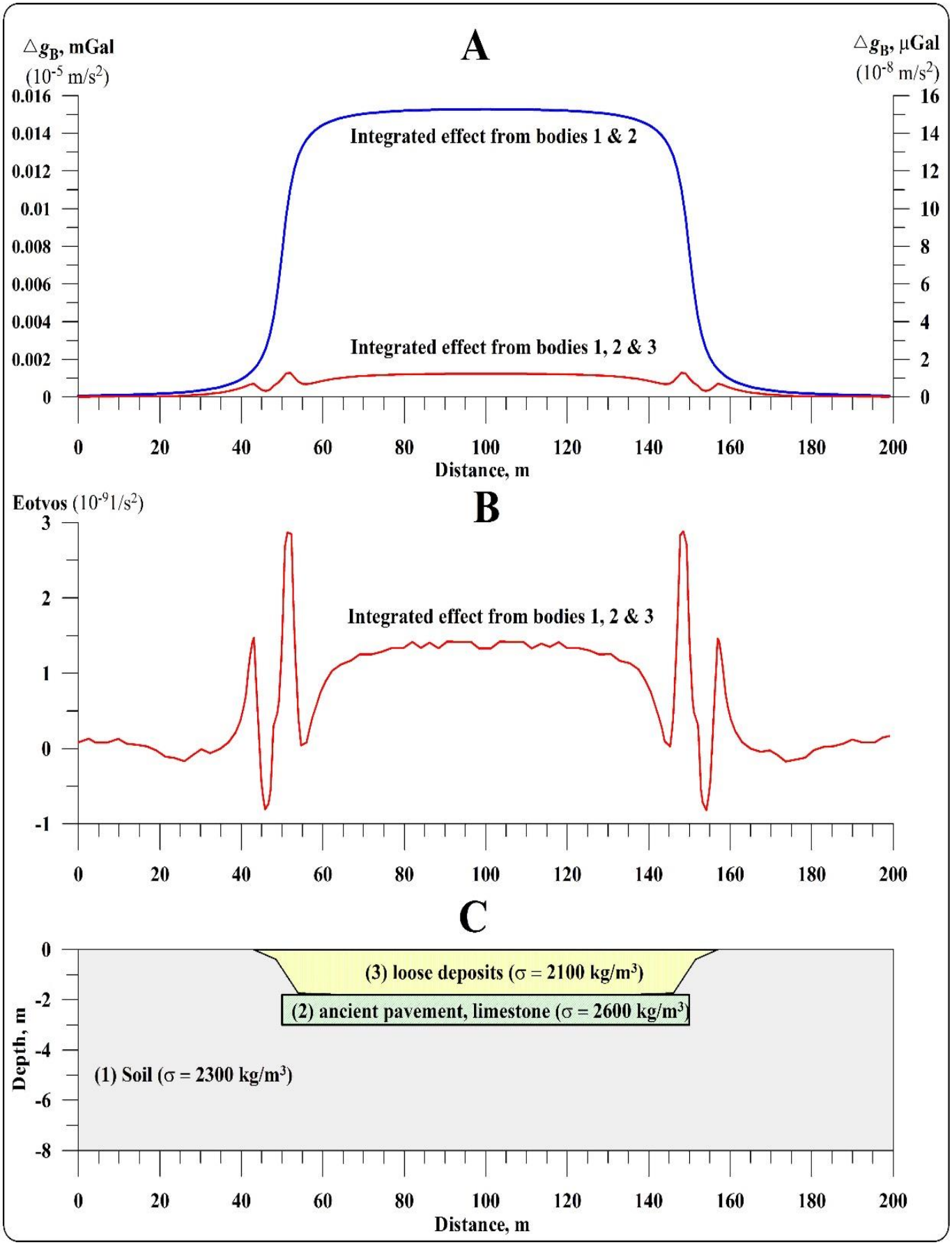

Figure 7. Comparison of Bouguer gravity and vertical gradient anomalies for a model of buried pavement. (**A**) Bouguer gravity, (**B**) vertical gradient g_z (W_{zz}) computed for the base of 1.2 m, (**C**) archaeological sequence (after [43])

Microgravity is one of popular methods for delineation of such dangerous geological phenomen as karst terranes [e.g., 16, 21-27].

Sometimes karst terranes occur at a close distance one from other (Figure 5). For their prompt identification, such a simple mean as calculation of the second horizontal derivatives of gravity field (g_{xx}) can be applied. Interestingly to note that a small positive gravity anomaly in Figure 5A, testifying presence of two anomalous bodies, can be recognized only with essential difficulties. Graph g_x shown in Figure 5B is more informative, but graph g_{xx} (Figure 5C) allows to fully recognize the form of the buried bodies (Figure 5D).

The Ghor Al-Haditha area is located in the northeastern Dead Sea basin (Jordan) where many karst terranes were developed during the last decades [26,28]. However, microgravity application in the areas closely disposed to the Dead Sea coasts are strongly disturbed by the greatest negative horizontal gravity gradient (Figure 6A) caused by accumulation of many km of loose deposits and salt within the Dead Sea Transform [24]. Analysis of different types of gravity gradient elimination allowed to select the local polynomial regression as the most effective method. Figure 6B displays the god fitting between the obtained residual gravity field (after removing the regional gradient background) and the results of 3D gravity field modeling over the buried sinkhole [26].

4.2.2. Cavities in lava flows and underground tunnels

Microgravity can also be effectively applied for delineation of cavities in lava flows [e.g., 29,30], and localization of underground tunnels [31-33].

4.2.3. Moon-Sun-Earth gravity system

Studying gravity fields of the Sun and Moon can help to predict the number of dangerous atmospheric events on the Earth. Eppelbaum [34] and Eppelbaum and Isakov [35] proposed to compute the tornado season prediction model based on the fast Fourier transform coefficients from the tornado spectrum, which coincide with the coefficients from the Sun–Moon–Earth gravitational/magnetic system. Proposed methodology was successfully tested on the number of tornado appearing in 2011-2015 seasons in the USA. Obviously, these and similar studies of the Moon-Sun gravity influence to the Earth's environment must be continued.

4.3. Archaeology

Numerous archaeological publications [e.g., 18, 36-44] indicate that the ancient objects supposed for examination by the use of microgravity survey may be classified (in the decreasing order of effectiveness) by the following way: (1) pyramids and compatible objects, (2) underground ancient cavities and galleries, (3) walls, remains of temples, churches and various massive constructions, (4) pavements and tombs, (5) Roman aqueducts [under favorable physical-geological environments], (6) areas of ancient primitive metallurgical activity (including furnaces) [under favorable physical-geological environments]. Examining the different archaeological targets in Israel, it was supposed that microgravity method might be effectively applied at least on 20-25% of the ancient sites [18]. Apparenty, in the world archaeology this number may consist of 15-20%.

It is necessary to underline that physical measurement of vertical gravity derivatives in many cases cannot be replaced by computing of this parameter obtained by any transformation procedures: the second vertical derivative of gravity potential W_{zz} values computed from the field Δg_B, as rule, show decreasing values comparing with the W_{zz} obtained from physical measurements. A simplified model example of buried pavement delineation (pavement excavated at the Megiddo site (northern Israel) was utilized as a generalized physical-geological model) is presented in Figure 7. A buried pavement having the positive density contrast of 400 kg/m^3 and occurring at a depth of 1.8 m in uniform medium could be easily recognized by

the microgravity survey (Figure 7A, anomalous effect from two bodies). Let us will assume a pavement (Figure 7C). It makes the delineation of the pavement practically impossible in field conditions (registered anomaly is oscillating about 1 microGal) (Figure 7A, anomalous effect from three bodies). At the same time, values of the second vertical derivative of gravity potential (W_{zz}) (computed for the levels of 0.3 and 1.5 m) with a measurable accuracy testify to presence of a disturbing body (Figure 7B).

4.4. Engineering monitoring

4.4.1. Monitoring of natural and artificial processes

Microgravity monitoring can be effectively applied for control of gas volume in natural and artificial reservoirs [e.g., 8; 45-47], inspection of the underground water levels [e.g., 48-50], and for computing of water flow geodynamics [e.g., 51].

4.4.2. Remote Operative Vehicle gravity survey

Employment of low-altitude Remote Operative Vehicle (ROV) could significantly extend the possibilities of gravity studies/monitoring, especially in such practically inaccessible areas as swamps, bush/forest, mountainous regions with severe relief, etc. Recent publication [52] proposes to employ chips gravity measurements at the near future. For increasing accuracy of positioning, a non-conventional Kalman filtering model with the wide-band noise model [20] can be applied. Besides this, prompt and low-cost multilevel gravity observations will meaningfully increase the horizons of interpretation.

4.5. Examination of geodynamic activity at a depth

It is known that very precise gravity measurements may be applied for investigation of geodynamic activity at a depth [e.g., 53-58].

4.6. Monitoring of volcanic activity

Monitoring of volcanic activity consists in revealing of newly arisen magma flows in the upper part of volcanic complexes and recognizing many other subsurface processes [e.g., 59-63].

4.7. Searching and localization of economic deposits

Gravity prospecting is effectively applied for searching and localization of ore deposits: iron, chrome, copper, sulphide, polymetallic, nickel, molibdenum, manganese; hydrocarbon accumulations; underground water horizons and some other types of economic deposits [e.g., 7,9,10,11, 14-16].

4.7.1. Ore deposits

The gravity method application for localization of ore bodies can be illustrated by a comprehensive gravity field examination in the Katekh polymetallic deposit (Filizchai ore field, northern Azerbaijan) (see its location in Figure 11). The deposit is situated in the southern slope of the Greater Caucasus under conditions of severe rugged topography. A combination of latitudinal and longitudinal faults strongly complicates the deposit structure. The Katekh deposit was investigated by mining and drilling up to a depth of 500 m. The main ore minerals of the Katekh deposit are pyrite, sphalerite, chalcopyrite and galena [64].

A 3-D combined modelling of Bouguer gravity (Δg_B) and vertical component of the total magnetic field ΔZ has been carried out using the following procedure. A detailed physical-geological model of the Katekh deposit (length = 800 m, depth = 400 m) has been constructed (Figure 8A). Then, all the available data for this area on density and magnetic susceptibility were utilized. For enhanced calculation of the surrounding terrain topography, a digital terrain relief model (DTRM) was created. The expressed SW-NE regional topography trend in low-density layer (2100 kg/m^3) over the

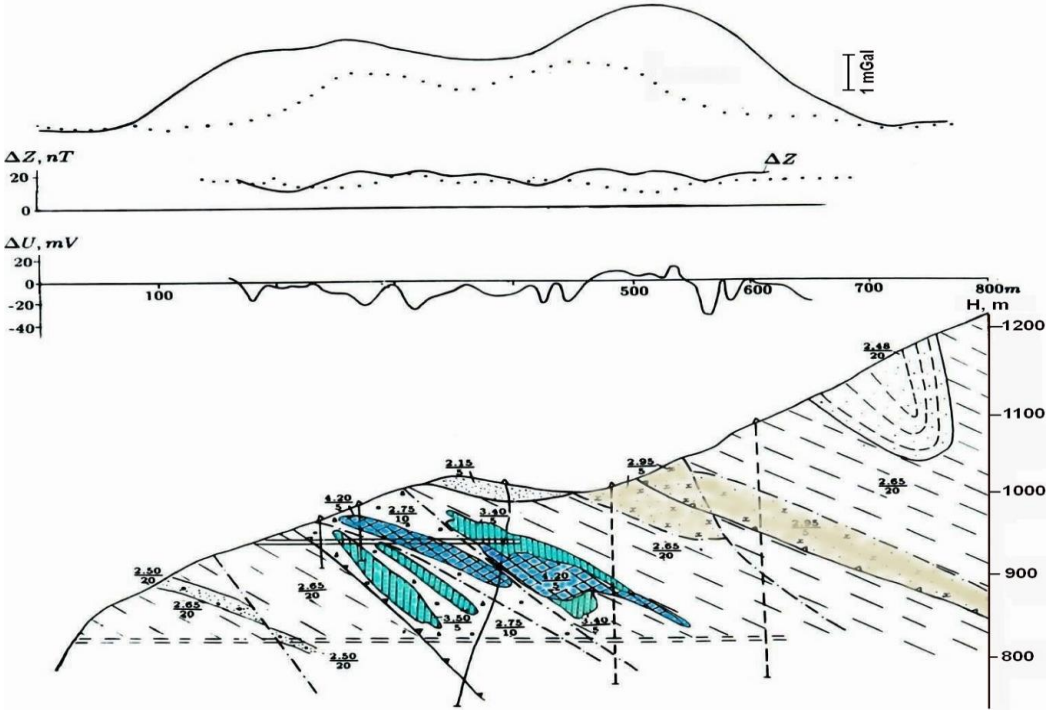

Figure 8a. Computation of gravity (i) and magnetic (ii) fields due to a known geological section in the Katekh pyrite-polymetallic deposit; (iii) presents results of self-potential method application (after [18], with modifications)

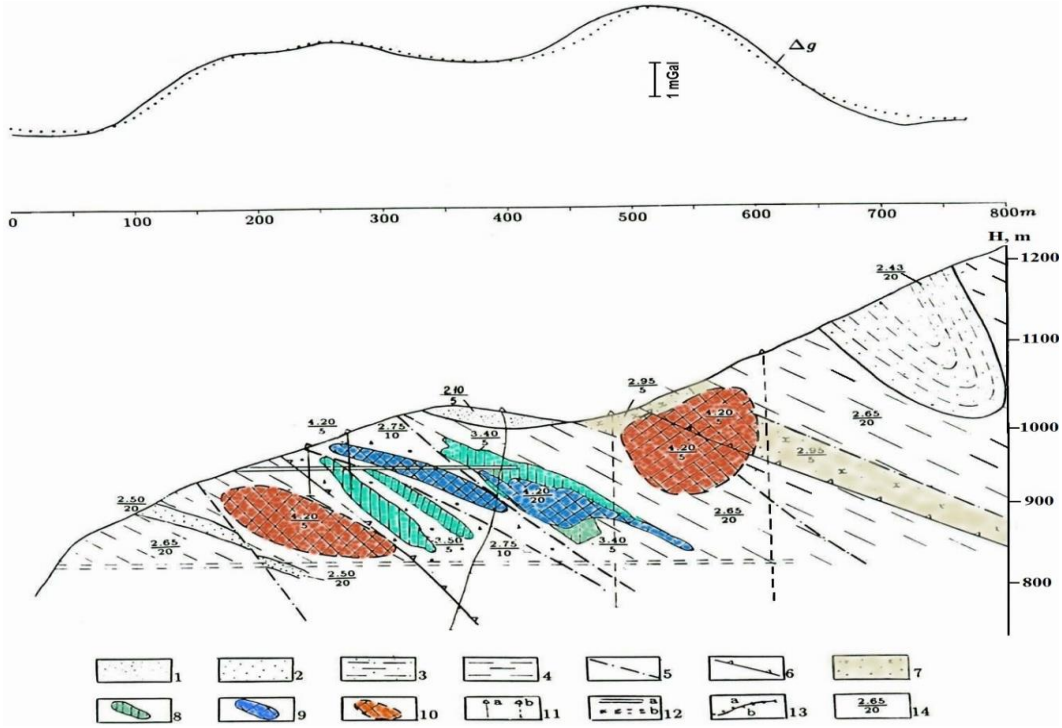

Figure 8b. (1) Quaternary loose deposits; (2-4) Middle Jurassic deposits: (2) massive fine- and meso-grained sandstones, (3) interbedding of shales and sandstones, (4) rhythmical alternation of siltstones and shales; (5) disjunctive dislocations; (6) upthrust-overthrusts; (7-9) pyrite-polymetallic ores: (7) spotty-disseminated, (8) veiny-clastic, (9) massive; (10) ore bodies introduced as result of 3-D gravity modeling; (11) prospecting boreholes: (a) in the profile, (b) projected to the profile; (12) adits: (a) in the plane of the geological section, (b) projected into the plane of the geological section; (13) graphs of gravity and magnetic fields: (a) observed (solid line), (b) computed (spots); (14) physical properties: numerator = density, g/cm^3, denominator = magnetization, mA/m (after [18], with modifications)

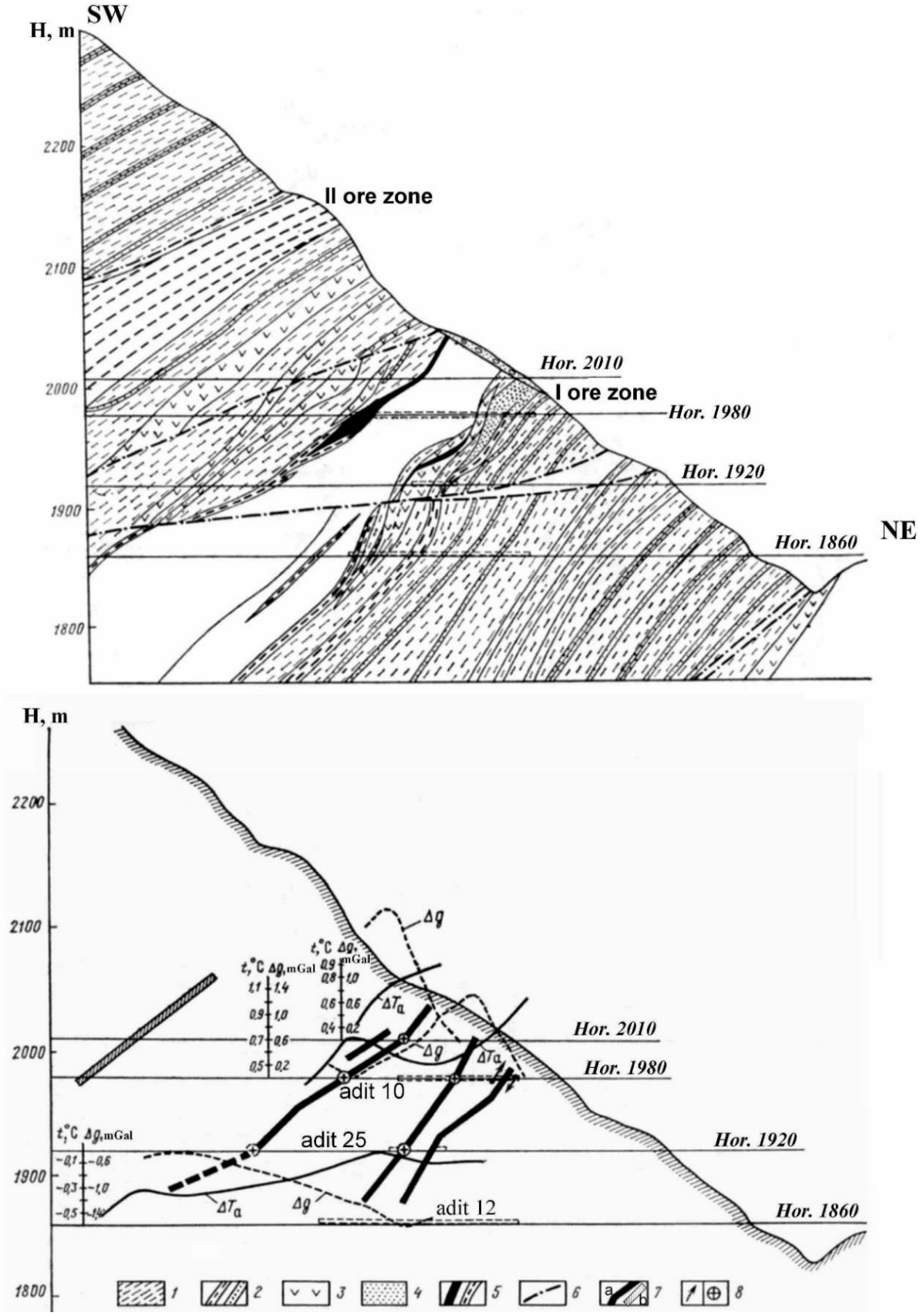

Figure 9. Integrated geophysical investigations in mines of Katsdag deposit (southern slope of the Greater Caucasus) (after [65], with modifications).(1) shales, (2) interbedding of shales, sandstones and siltstones, (3) dioritic porphyry, (4) oxidizing zone, (5) polymetallic ores of I and II zones, (6) faults, (7) apparent beds of redundant: density (**a**) and thermal conductivity (**b**), (8) current axes revealed by the VLF method

the area of the Katekh deposit led to the selection of a DTRM with a length of 20 km and a width of 600 m (the physical-geological profile with a length of 800 m was located in the geometric center of the DTRM). Overall, 1,000 characteristic points describing the DTRM (with these points located close to the center of the DTRM and more rarely on these margins) were utilized.

The results of the first iteration of the gravity-magnetic fields modeling indicate in that the plots of ΔZ and ΔU_{SP} (self-potential anomalies) are non-informative ones (Figure 8A). This is due to the peculiarities of the mineralogical composition: the practical absence of magnetic mineral pyrrhotite causes the non-magnetic nature of the ores; the large lead content hampers the oxidation-reduction reactions needed to trigger of intense SP anomalies. Thus, crucial geophysical information can only be derived from the gravity field analysis. The analysis of the observed and computed gravity fields (Figure 8A) shows that the initial physical-geological model has a certain deficit of anomalous masses. 3-D gravity field modeling was carried out by the use of about 35 sequential iterations. It yielded the following results (Figure 8b): two massive ore bodies were discovered in the southwestern and northeastern segments of the deposit. The conclusion as to the presence of a hidden ore object in the southwestern portion of the profile is consistent with the results of independent investigations. A temperature anomaly of 0.5–0.8 ^{o}C was recorded in the adit 8 during the underground geothermal investigations at 250–300 m; the surface zone containing a large amount of lead and zinc was revealed at 150–200 m of the section.

An example of the underground gravity survey combined with thermal and VLF data examination (the author, as a student in the Geophysical Dept. of the Azerbaijan Univ. of Oil & Chemistry, took part in these field works) in the Katsdag polymetallic deposit is presented in Figure 9. The Katsdag polymetallic deposit is a part of the Filizchai ore field situated in the southern slope of the Greater Caucasus (see Figure 11). It located in conditions of severe rugged relief; the main geological tool of this deposit investigation were several mines and boreholes. Employment of gravity survey in mines integrated with other geophysical methods enabled to delineate earlier unknown ore bodies [65]. The peculiarities of the underground gravity studies are given, for instance, in [66].

Interestingly to note that detailed gravity-gradient examination of V.I. Segalovich enabled to discover in the 1960s a rich chrome deposit in the Kempersai area of Kazakhstan [8].

4.7.2. Hydrocarbon deposits

Effective examples of calculation of the second vertical derivatives of gravity field for delineation of anticline structures in hydrocarbon-bearing areas of Texas and Oklahoma are shown in [67].

Proposed by Berezkin [68] the total gradient method (complex nonlinear filter band-pass filter) of gravity data processing has shown to be effective to delineate the hydrocarbon deposits in Russia, Kazakhstan, South Caucasus, Near and Middle East and in other regions of the world.

Tzimelzon [69] in the Middle Kur Depression (Azerbaijan) (see Figure 11) performed one of effective gravity survey examinations in hydrocarbon geophysics. His gravity data analysis permitted firstly to discover the Muradkhanly anticline structure (Figure 10) where afterwards a rich oil deposit was discovered. Later Gadirov and Eppelbaum [70] unmasked the composition of the Muradkhanly gravity anomaly by the way of its subdivision to separate components.

4.8. 3D combined gravity-magnetic field modeling

4.8.1. Azerbaijan and South Caucasus

The complexity of Azerbaijan's territory geological structure is caused by its location within the Alpine-Himalayan Tectonic Belt

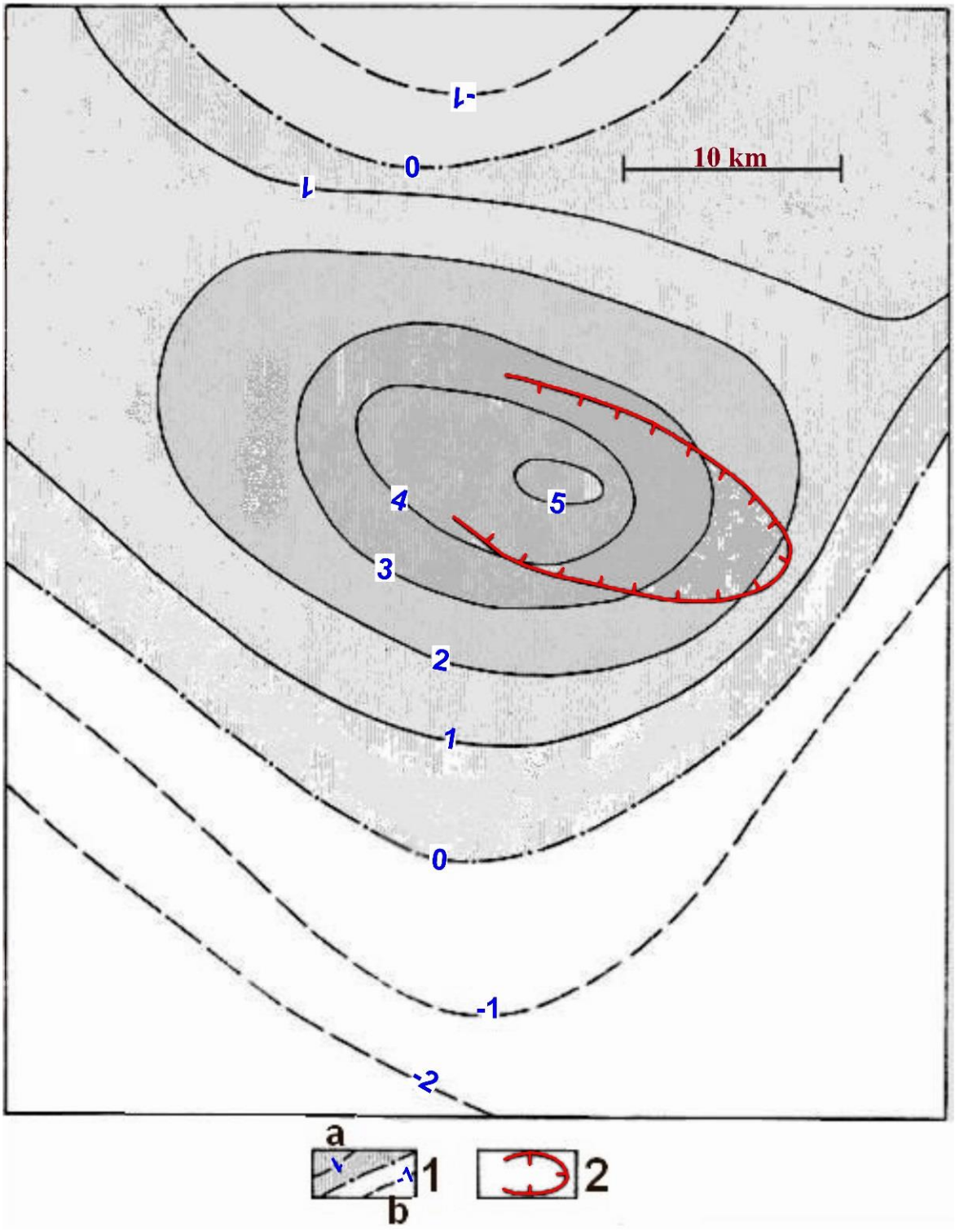

Figure 10. Gravity method as a successful tool for delineation of the buried Muradkhanly structure (after [17,69] (1) difference gravity field $\Delta g_{B(0\text{-}10)}$, mGal: (a) positive, (b) negative; (2) contour of the Muradkhanly uplift according to seismic prospecting data and results of drilling.

Note. $\Delta g_{B(0\text{-}10)}$ is the difference between the gravity field in the Bouguer reduction observed at the earth' surface and analytically continued to the level of 10 km.

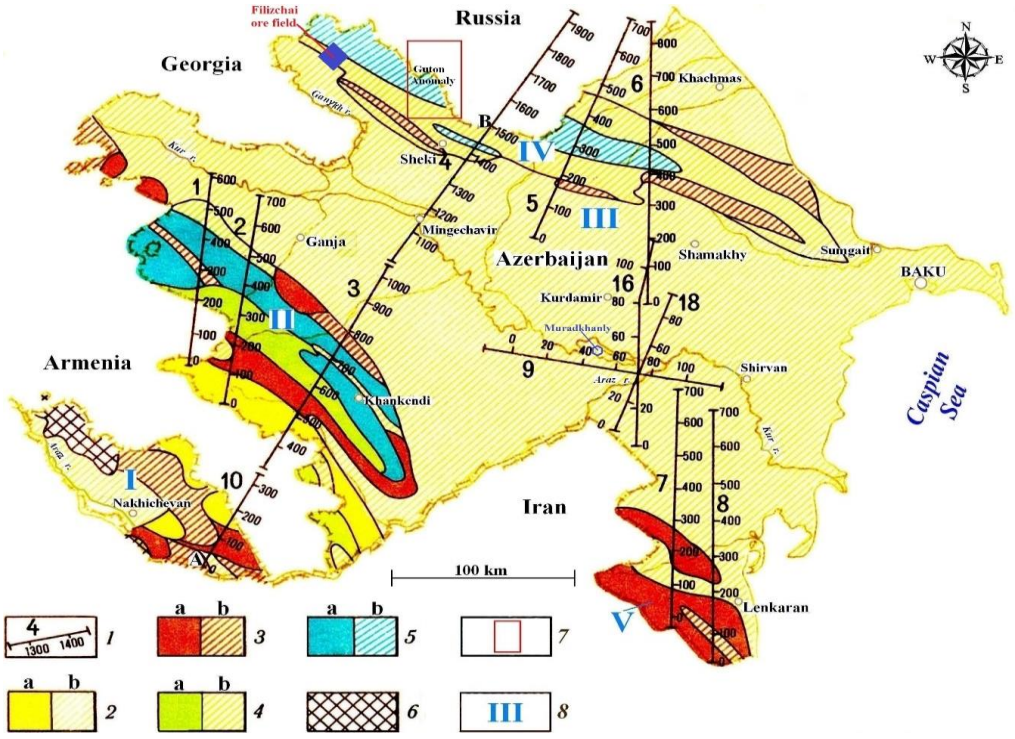

Figure 11. Areal map of some profiles used for physical-geological modeling in Azerbaijan and adjacent regions (after [72], with small modifications) (1) profiles and pickets, (2) Pg_3-Q: (a) orogenic magmatic associations, (b) background sedimentary deposits, (3) K_2-Pg_2: (a) pre-orogenic magmatic associations, (b) background sedimentary deposits, (4) J_3-K_1: (a) magmatic associations of the Late Alpine sub-stage, (b) background sedimentary deposits, (5) J_1-J_2: (a) magmatic associations of the Early Alpine sub-stage, (b) background sedimentary deposits; (6) Pz deposits, (7) contour of the Guton magnetic anomaly, (8) tectonic regions: I – Nakhichevan folding region, II – SE part of the Lesser Caucasus mega-anticlinorium, III – central and SE parts of the Kur mega-synclinorium, IV – SE part of the Greater Caucasus mega-anticlinorium, V – Talysh anticlinorium

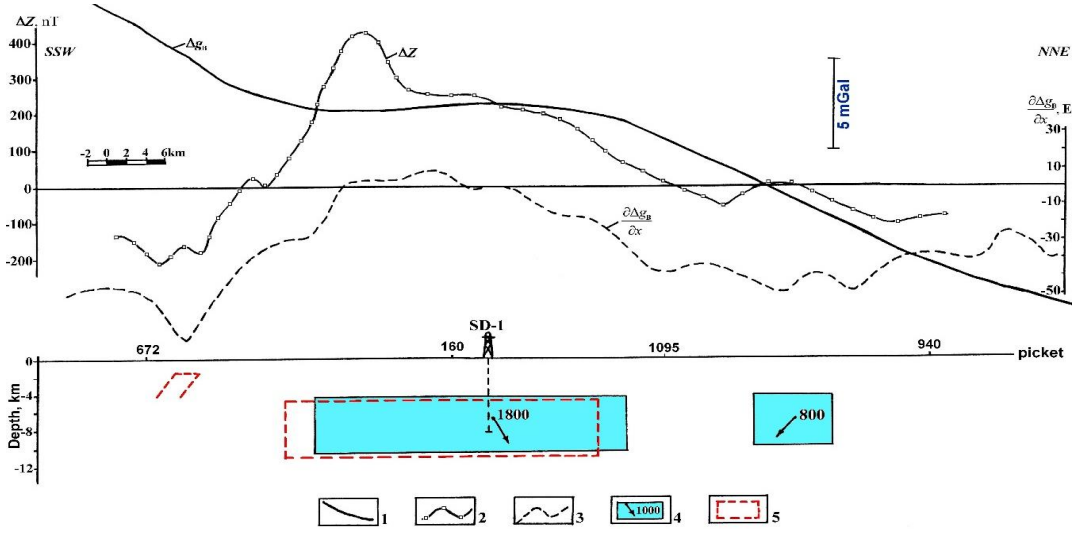

Figure 12. Fragment of gravity and magnetic field analysis along profile 18 (location of this profile is shown in Figure 11) (after [72, with modifications) (1) Bouguer gravity field Δg_B, (2) magnetic field ΔZ, (3) first horizontal derivative of gravity field $\partial \Delta g_B / \partial x$, (4) contour of magnetized body, magnetization and position of magnetization vector, (5) contour of body determined by analysis of $\partial \Delta g_B / \partial x$

(AHTB) [e.g., 64,71,72]. The NE part of Azerbaijan is a fragment of the Pre-Caucasian foreland composed by Cenozoic terrigenous sediments. Carbonate Paleozoic strata and Cenozoic magmatic formations are mixed in the heterogenic Nakhichevan folding system located in the SW part of Azerbaijan (Figure 11). Stratified Cenozoic and Mesozoic thick (predominantly, sedimentary) strata are presented at the mega-anticlinorium of the Greater Caucasus. The prevalence of Mesozoic magmatic formations is typical for the mega-anticlinorium of the Lesser Caucasus. The Kur mega-synclinorium, divides the Greater and Lesser Caucasus and characterizes by an accumulation of thick (up to several kilometers) Cenozoic terrigenous sediments. The Talysh anticlinorium with a wide distribution of Paleogene magmatic associations is situated on the SE flank of the Kur depression [64].

The most ancient pre-Baikalian (pre-Cadomian) structural complex is characterized by a sub-meridional strike [73]. A less metamorphosed Baikalian complex is rumpled to latitudinal folds in separate areas. The Caledonian complex is practically unknown. The Hercynian complex is characterized by a Caucasian strike alike to the overlying Mesozoic rocks.

The Alpine tectono-magmatic cycle is distinguished by more complete geological data. For Azerbaijan territory is generally typical frequently changing of rocks both on vertical and lateral, presence of multifarious fold and fault structures of different orders, regional and local metamorphism [64]. All these factors complicate development of the reliable physical-geological models of the region under study.

Advanced interpretation methods (improved modifications of tangents, characteristic point methods and areal method) were employed to examine gravity and magnetic anomalies along all profiles crossing and surrounding the SuperDeep borehole (SD-1) in the Saatly area of Azerbaijan (Figure 11). Figure 12 shows a fragment of this interpretation along Profile 18. It is clear that the behavior of the magnetic ΔZ curve and graph $\partial \Delta g_B / \partial x$ are very simular, which testifies to the fact that these anomalies are produced by the same geological targets. Quantitative examination of magnetic curve ΔZ enabled to delineate two magnetic objects. The main target speciously is a source of the Talysh-Vandam gravity anomaly (TVGA) (its upper surface agrees with the data obtained from SD-1 drilling) [64]. The obtained data were utilized at the stage of construction of Physical-Geological Model (*PGM*) of a first approximation [16].

Figure 13 shows an integrated key *PGM* (gravity + magnetic + seismic + thermics) of the deep structure along profile No. 9. This PGM clearly indicates the main sources of gravity and magnetic anomalies in this area. Obviously, the main source of the TVGA is associated with the underlying highly dense, strongly metamorphosized (initially chiefly sedimentary associations) non-magnetic or low-magnetic Pre-Baikalian (Pre-Cadomian) stage (this stage has a submeridional strike in the Russian and Nubian plates) [17]. The depth of the upper edge of these highly dense rocks was estimated at 9.5 km. An example of 3D combined modeling of gravity and magnetic fields along Profile 1 (see scheme of profiles presented in Figure 11) is shown in Figure 14 [74]. Profile 1 crossing the Lesser Caucasus indicates the very intricate geological structure of this region. The Late-Alpine effusives in the *PGM*s reflect an ophiolite zone (ancient ocean crust). It is thought that the same geological associations occur in the north-east immersion of the Lesser Caucasus. In the southern part of the *PGM* pre-orogenic and orogenic intrusive and effusive rocks are fixed. In the northern part of this profile thick sedimentary deposits are developed. The Moho discontinuity is smoothly uplifted from south to north from a depth of 52 km up to 42 km [72]. Such a Moho boundary behavior overall agrees with the latest data of the deep seismic profile re-

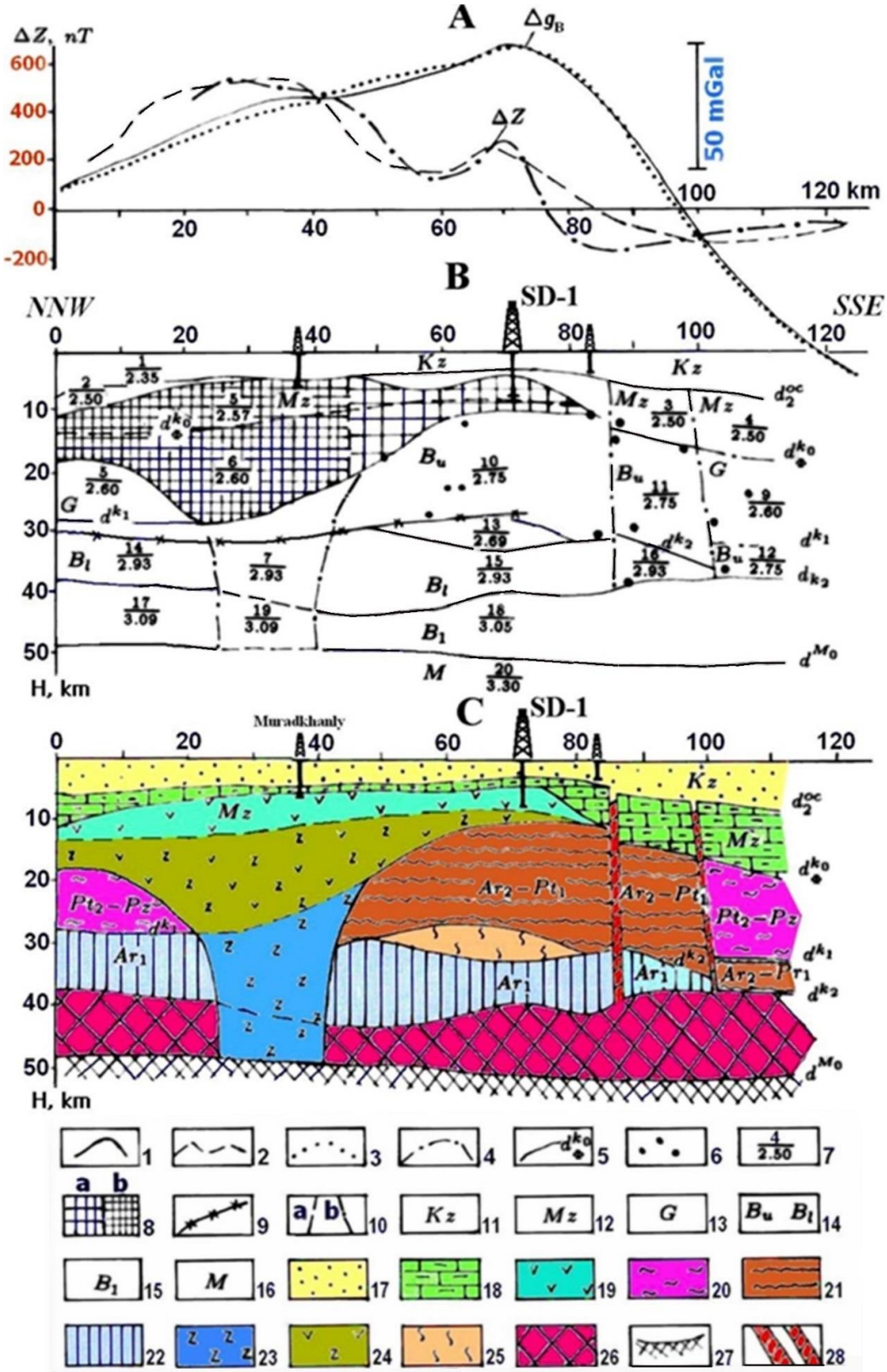

Figure 13. Deep geological section of the Earth's crust in SD-1 area along profile 9 (location of this profile is shown in Figure 11) (after [74], with small modifications) **A**: gravity and magnetic fields observed and computed for model **B**; **B**: petrophysical model, **C**: geological model Observed fields: (1) $\Delta g_{\mathbf{B}}$, (2) ΔZ; fields computed from the model **B**: (3) Δg_{B}, (4) ΔZ; (5) boundaries of the velocity and the density heterogeneities and their indices, (6) diffraction points, (7) body number (numerator) and density value, g/cm^3 (denominator), (8) geological bodies with the magnetization of 2,500 mA/m (a) and 2,800 mA/m (b), (9) projection of the Curie surface constructed on the basis of geothermal data analysis, (10) sub-vertical boundaries obtained by the use of magnetic (a) and gravity (b) field modeling, (11) Cenozoic, (12) Mesozoic, (13) *G* complex (velocity

analogue of the “granitic” layer), (14) B_u and B_l subcomplexes of *B* complex (complex *B* is the “basaltic” layer velocity analogue), (15) B_1 complex (presumed basite and eclogite composition), (16) *M* complex (presumed peridotite composition), (17) Cenozoic complex: mainly terrigenous deposits, Mesozoic complex: (18) terrigenous-carbonaceous formations, (19) mainly effusive associations of basic and intermediate composition, (20) mainly Baikalian (Cadomian) complex (Pt_2-Pz): metamorphic (primarily terrigenous) associations (the presence of younger deposits is possible in the upper part), (21) Pre-Baikalian (Pre-Cadomian) complex (Ar_2-Pr_1): mainly gneisses and marbles, (22) ancient complex (Ar_1): gneisses and amphibolites, (23) root of the basic magmatism, (24) undivided effusive-intrusive complex, (25) rock complex of a low density (serpentinization zone **?**), (26) complex of associations corresponding to the crust-mantle transition, (27) upper mantle roof position, (28) large fault zones

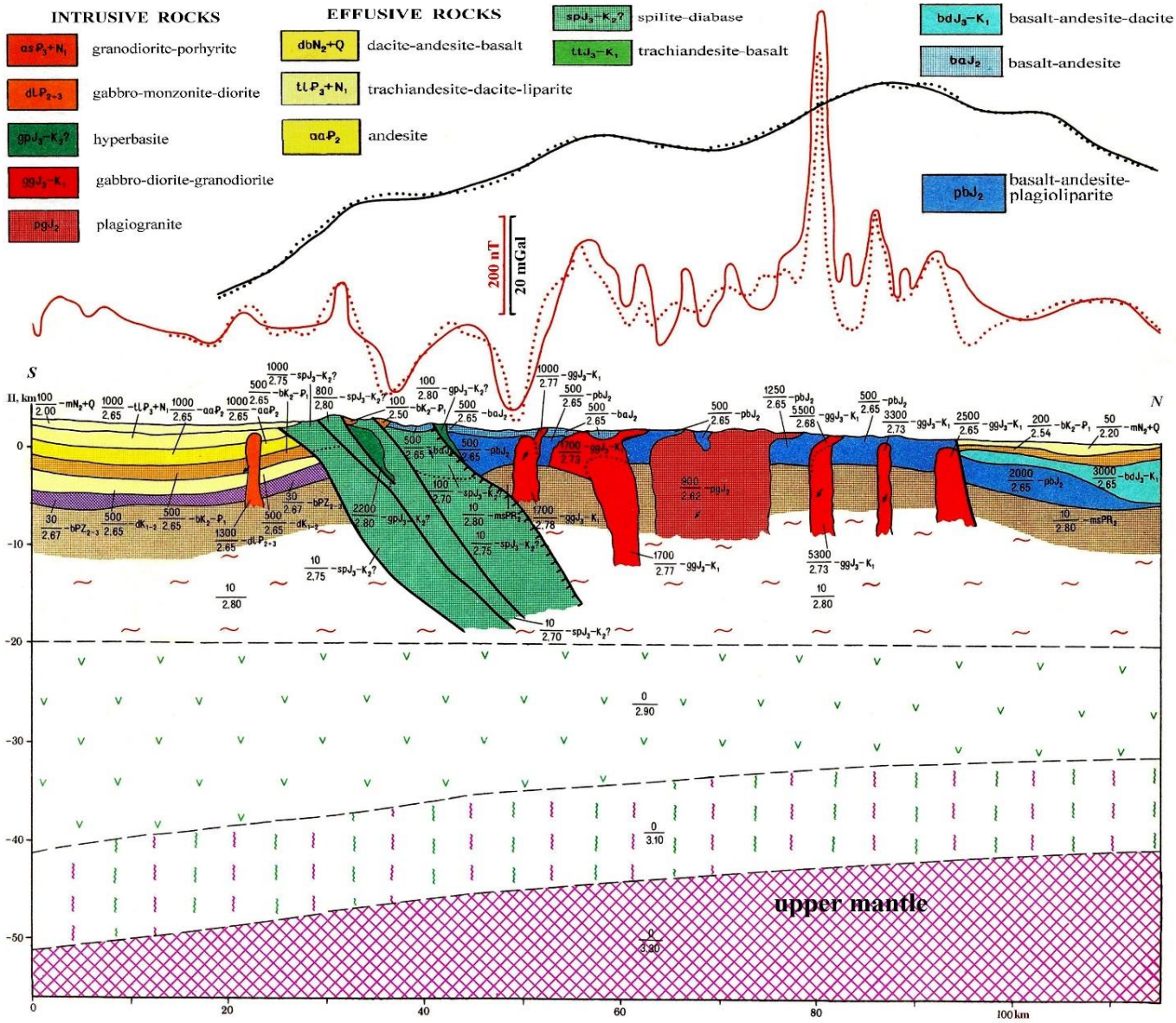

Figure 14. Physical-geological model along Profile 1: Mez-Mazra – Kedabek - Dzegam-Djirdakhan (location of the profile is shown in Figure 11) (after [74], with modifications). Description of sedimentary rocks is omitted for simplicity. Solid red and black lines show observed magnetic, gravity fields, and red and black dots – computed magnetic, gravity fields, respectively.

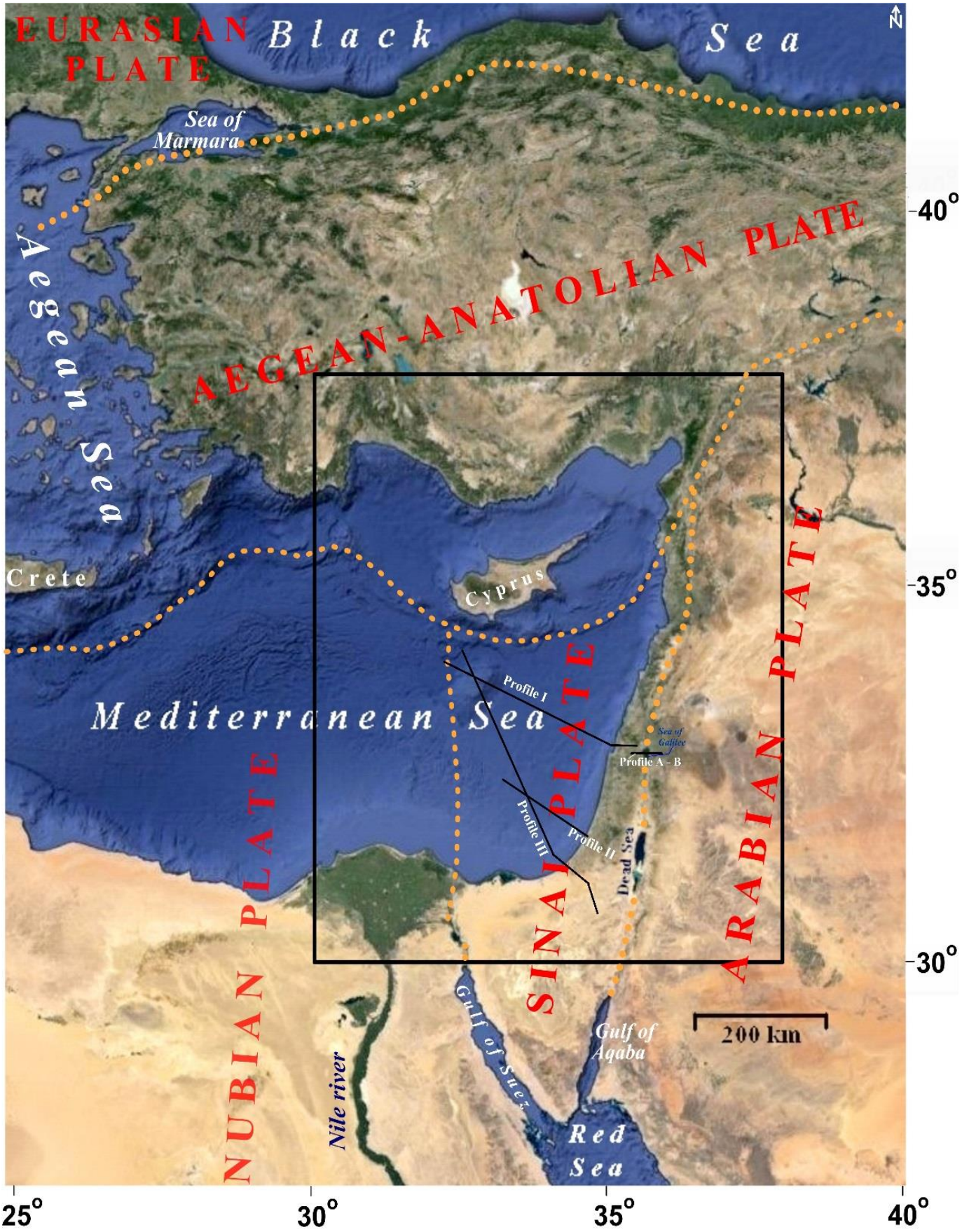

Figure 15. Overview map of the region. The study area is outlined by a black rectangle. Orange dot lines indicate boundaries between tectonic plates

interpretation [75]. Depths of the magnetized bodies' lower edges were estimated based on various geophysical field analyses [76]. Here were recognized such classes of anomalous objects as acid intrusions of lower density/magnetization, basic magmatic rocks of heightened density/magnetization, and fault zones of different order. It was found that the contrast density boundaries are associated mainly with the base of the Cenozoic sedimentary strata and, to a minor degree, with the base of the Alpine complexes. The results of carried out 3D magnetic-gravity modeling indicate that geomagnetic boundaries are associated mainly with the roof and bottom of the Mesozoic stage.

4.8.2. Eastern Mediterranean

3D combined gravity-magnetic modeling has been successfully performed along seismic profiles I, II and III in the Eastern Mediterranean [77]. Location of these profiles accompanied by some tectonic setting is shown in Figure 15. Example presented in Figure 16 displays the final *PGM* along the profile crossing the Sea of Galilee (profile A – B) developed by the use of 3D combined gravity-magnetic field modeling (location of this profile is presented in Figure 15). A preliminary *PGM* of this profile was constructed on the basis of [78-84].

The preferences of integrated gravity-magnetic-paleomagnetic analysis are clearly demonstrated in Figure 16. Negative gravity anomaly along profile A – B (Figure 16-I) is caused mainly by the low dense sedimentary deposits and salt accumulations in the Dead Sea Transform zone within the Sea of Galilee. Such a model in general agrees with the seismic data. At the same time, comprehensive analysis of magnetic field behavior indicates that it cannot be explained by subsurface basalts effects (and by effects from any basaltic plates occurring at low depth) (Figure 16-II). Such a behavior may provide only a deep crystal block with an inverse magnetization (Figure 16-IV). A crystal (basaltic) block with the similar direction of magnetization was discovered earlier in the eastern part of profile I in the Eastern Mediterranean [77]. Petrographic and radiometric analyses of the Sinai and Arabian shields (see Figure 15) indicate that here occur various complexes of Middle and Upper Precambrian among which dominate Neoproterozoic associations with a radiometric age of 600 – 1000 Ma [e.g., 85,86]. Numerous paleomagnetic examinations of Neoproterozoic display that in those rocks an inverse magnetization is prevailing [87,88]. A generalized paleomagnetic scale of Neoproterozoic (reconstructed by Y. Katz based on the numerous paleomagnetic determinations analyses) is demonstrated in Figure 16-III. Simple visual analysis of this scale indicates that the most intervals of the magnetic field inverse polarization relate to 605 – 815 Ma. Thus, we can relate the discovered zone of inverse magnetization (taking into account the results obtained for profile I [77] and profile A – B (Figure 16)) (see the brightly yellow colored block) to Neoproterozoic (interval about 210 My, between 605 and 815 Ma).

4.9. Satellite derived gravity field analysis

4.9.1. Eastern Mediterranean

The Eastern Mediterranean is tectonically very intricate region located in the midst of the progressive Afro-Eurasian collision. Its geological-geophysical structure has been intensively investigated last 100 years but is still not fully understand. The Eastern Mediterranean represents a classic region for the plate tectonics interaction [e.g., 77; 89-99]. In addition, the discovery of significant hydrocarbon deposits in this region [e.g., 100-102] in the last years clearly underscore the need for new regional tectonic-structural substantiation of hydrocarbon structures to support the prospecting.

The findings showed that the new generation of the satellite derived gravity data could be used effectively for tectono-geological mapping [e.g., 97,98, 103-106]. The satellite gravity data were

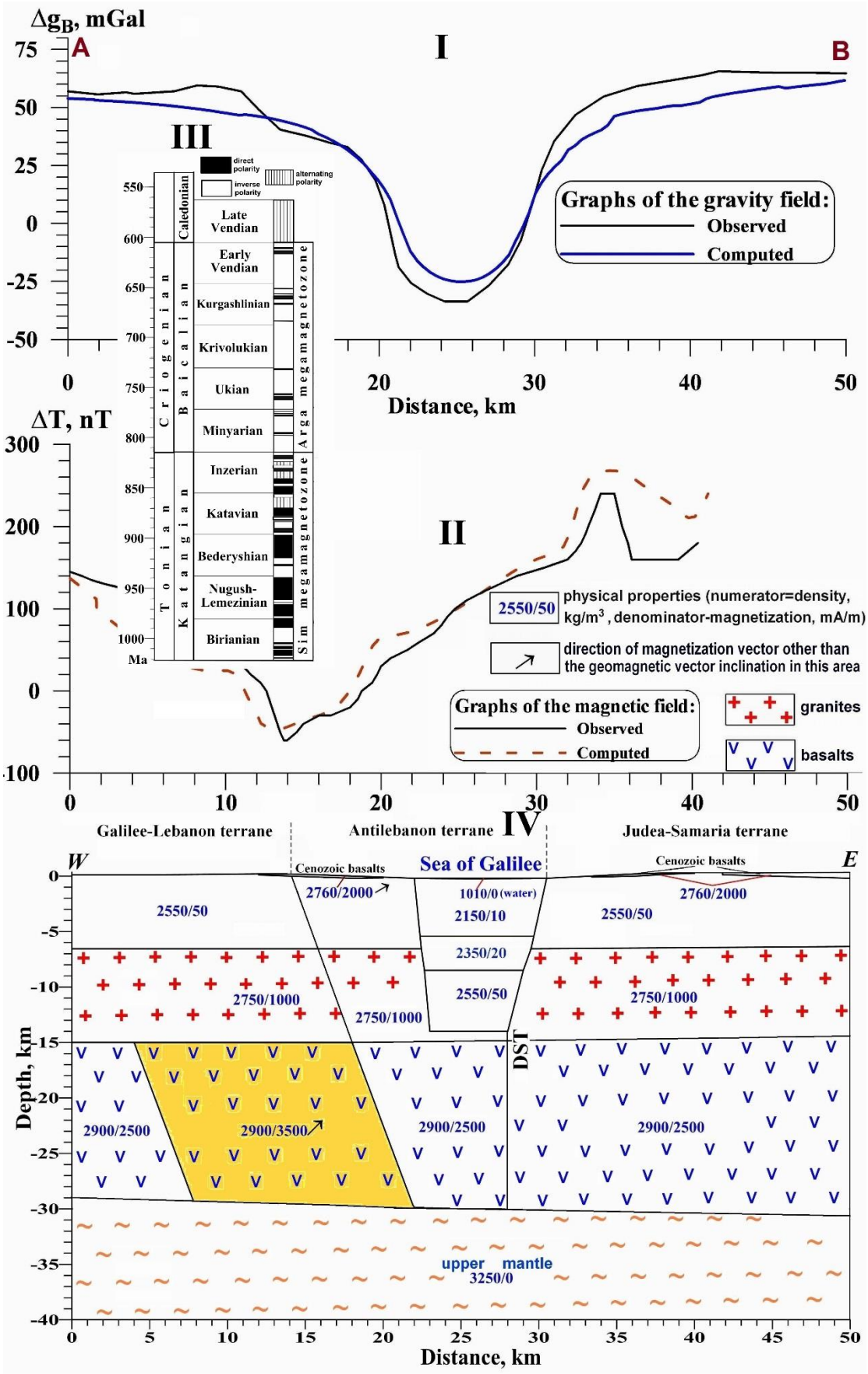

Figure 16. Combined ***PGM*** constructed on the basis of 3D gravity-magnetic modeling and seismic data analysis along profile A – B (location of profile A – B is shown in Figure 15). Terranes Galilee-Lebanon, Antilebanon and Judea-Samaria are shown also in Figure 18. I: Results of 3D gravity field modeling, II: Results of 3D magnetic field modeling, III: A generalized paleomagnetic scheme of Neoproterozoic, IV: Physical-geological model (after [72], with significant modifications).

obtained from the World Gravity Data Base as retracked from the Geosat satellite and ERS-1 altimetry [107]. It should be noted that these observations were made with regular global 1-minute grids [4,107] and the gravity data computation error was estimated at 1 mGal. Without hesitation, the enormous amount of satellite derived gravity data (from various satellite missions) and their extraordinary variety clearly make these observations fall into the category of 'big data' [e.g., 108,109].

The gravity map compiled in Figure 17 shows the intricate gravity pattern of this area (the isoline interval is 5 mGal; “zero” isoline is dashed and bolded). The positive and negative gravity anomalies (Figure 17) clearly reflect the majority of the structural-geotectonical units of the region. The map depicts both the main structural elements (e.g., Eastern Mediterranean basin), and the smaller depressions and highs of the neotectonic relief of the Nubean-Arabian and Anatolian plates.

The map of first directional derivatives of the satellite-derived gravity field in a south-north direction is shown in Figure 18 (see also black rectangle in Figure 15). This direction was selected because the most geological structures in the Alpine Mediterranean belt area are characterized mainly by east-west extension [110,111] including the Mesozoic terrane belt [97,112]. The derivatives trace the main tectonic and geophysical features of the region, especially the boundary between continental and oceanic crust (revealed in [77]). The arcuate structure of the Alpine belt is distinct relative to trends in oceanic crust of the easternmost Mediterranean and in the Mesozoic terranes. In the main Alpine belt, the Taurids, South Taurids and Anatolides, terranes are visibly separated. Similarly, the Herodotus basin, west of the Eratosthenes Continental Block [102], together with the northern Mediterranean Ridge, outline a domain distinct from the Levantine Basin.

4.9.2. Arabian-African region

The Arabian-African region is of pronounced interest from many points of view: geodynamically (high seismic activity, active rift zones and collision processes), structurally (presence of mosaic block system of continental and oceanic Earth's crust of different age), geophysically (presence of several greatest gravity anomalies and intricate magnetic pattern) and economically (occurrence of the main hydrocarbon resources of the world).

The studied area (coordinates: 0^o – 38^o North, and 30^o – 57^o East) occupies a huge region of the Near and Middle East and Eastern-Northern Africa. This area extends for almost 13 million km^2 and examination of its tectonic and geodynamic features is of high importance [103, 112].

Employment of the multidimensional statistical analysis (MSA) (Figure 19) is performed by the use of sliding window of adaptive rectangular/inclined form (it enables to compute effects from the geological targets with different locations along the strike); background gravity field was automatically detected. MSA calculation has been performed by the use of the KOSKAD software [113].

MSA implementation to the satellite derived gravity data enabled not only to delineate geodynamical parameters of the studied region (collision zone at the boundary between the Arabian and Eurasian Plates, and active rift zones between the Arabian, Nubian and Somalian Plates, etc.), but also to estimate some tectonic characteristics of the Earth's crust (Figure 19). The MSA map clearly shows zone of development of the oceanic crust of the Easternmost Mediterranean and zone of oceanic crust of the Gulf of Aden and eastern (oceanic) part of the Somalian Plate. Besides this, in this map the Arabian and East African active rift zones as well as collision zone between the Arabian and Eurasian Plates are visibly traced. Entropy calculation has been

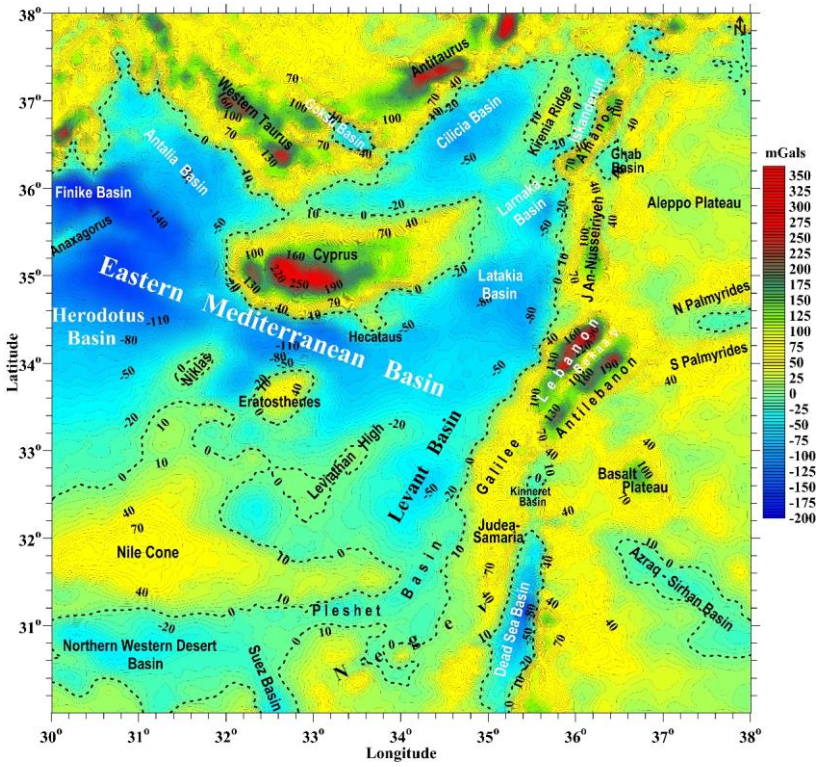

Figure 17. Map of key satellite derived gravity anomalies of the Eastern Mediterranean (modified and supplemented after [99]).

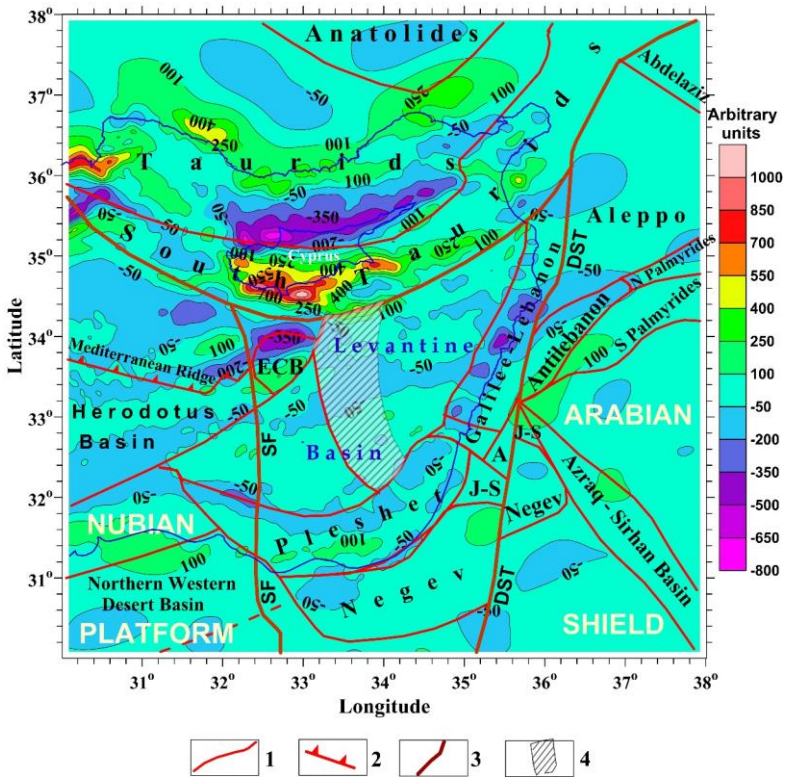

Figure 18. Map of spatial derivatives of the satellite derived gravity field of the Eastern Mediterranean (after [99], with modifications). (1) intraplate faults, (2) southern boundary of the Mediterranean accretionary belt, (3) main faults, (4) contour of the Kiama paleomagnetic zone. Blue line shows boundary between the Mediterranean Sea and land. ECB, Eratosthenes Continental Block, A, Antilebanon, J-S, Judea-Samaria, SF, Sinai Fault, DST, Dead Sea Transform.

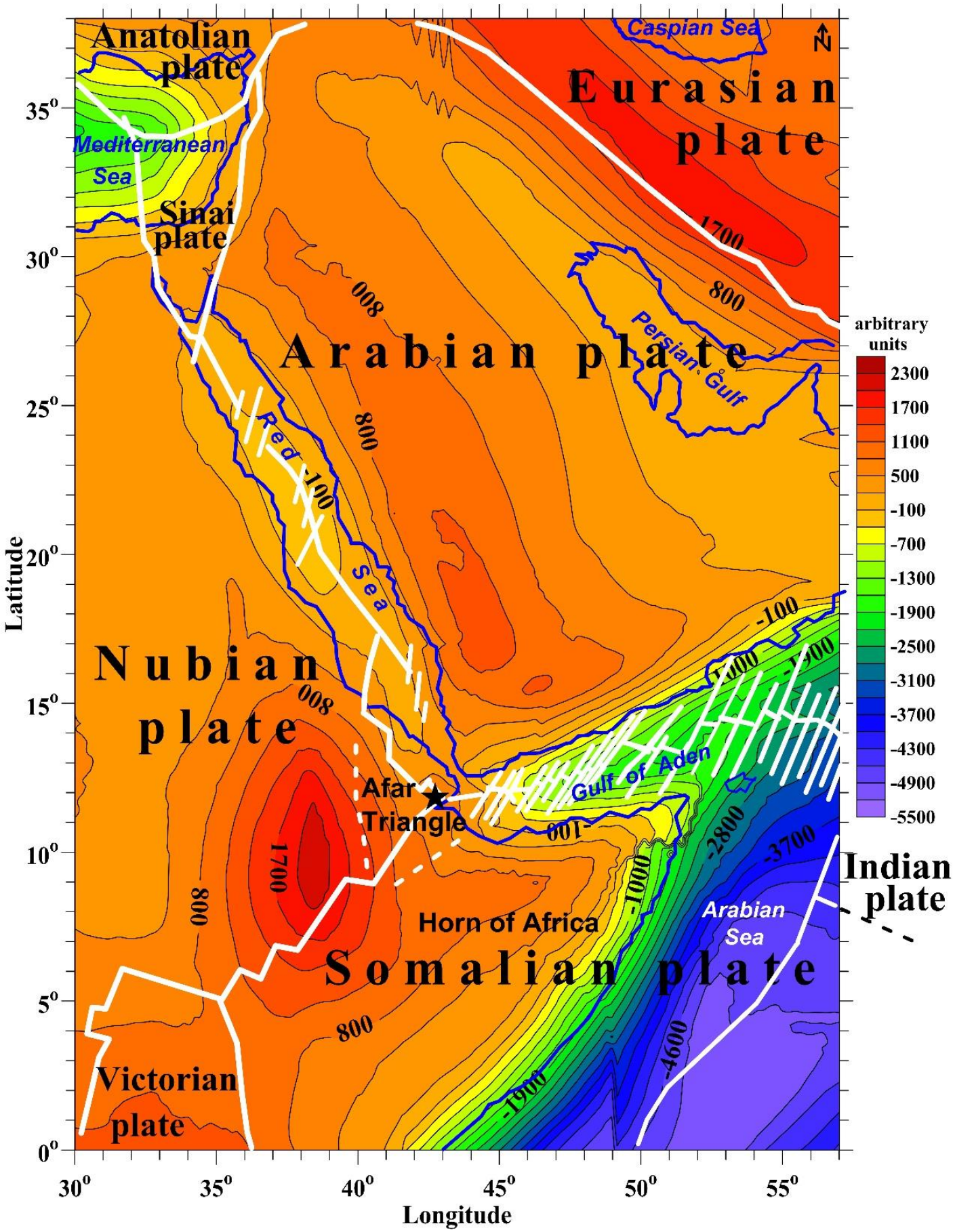

Figure 19. Map of satellite derived gravity field transformed by use of the multidimensional statistical analysis supplemented by main plate tectonics units (after [103], with modifications). White lines indicate fault systems, and blue lines show boundaries between the land and marine areas.

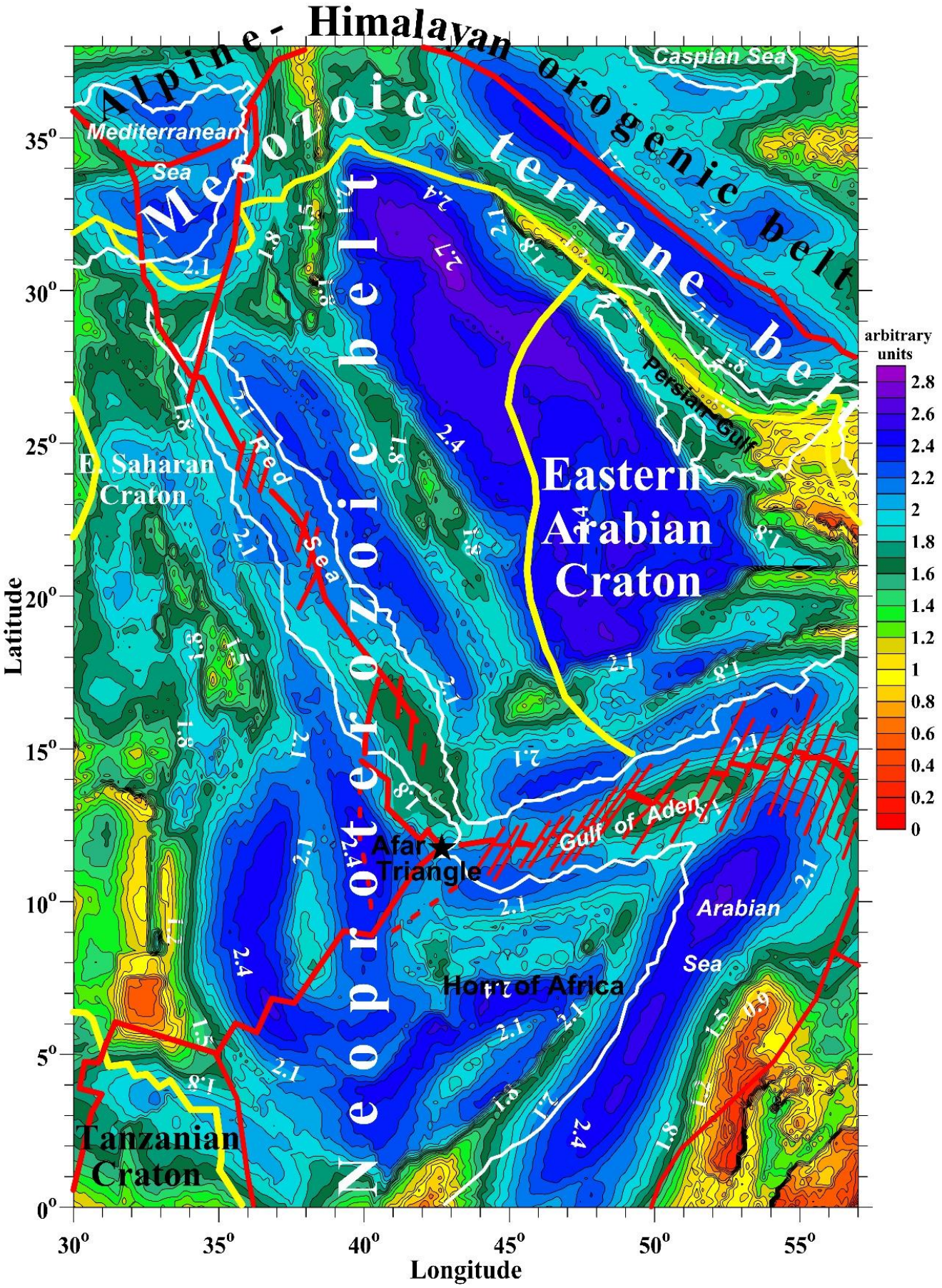

Figure 20. Entropy map accompanied by general tectonic features (after [112], with modifications). Red lines indicate fault systems; yellow lines show boundaries of cratons and tectonic belts; white lines show boundaries between the land and seas (ocean).

carried out by the use of the KOSKAD software [113].

Obviously, computing an entropy map (Figure 20) reproduces mainly deep tectonic elements of the region. Complex patterns of the entropy field in the SE part of the region reflect the transfer of mass from the Somalian Plate to the Indian Plate (this area is characterized by the most highly mosaic pattern). The entropy map analysis shows that the increase in entropy values corresponds to an elongation from the South to the North zone of ascending tectonic movements relating to the African-Arabian rift systems. This feature's formation may be explained by the fact that the lowest entropy values emerge in the near-equatorial zone at latitudes of 0 – 7.5^{o} to the North, and the largest values appear at latitudes of 30 – 35^{o} to the North; i.e., nearly the critical parallel zone of the conjugate deformation of the Earth's ellipsoid [114].

5. Further Ways of Gravity Data Evaluation

Analysis of gravity method evolution enabled to formulate the most perspective ways of gravity data in the near future:

(1) 3D gravity (and combined gravity-magnetic) field modeling will continue to be a powerful tool in the hands of interpreter with a good knowledge of geological disciplines.

(2) Development of modern transformation methods for gravity field processing will produce new comprehensive knowledge about the Earth's structure and subsurface, especially for complex geological sections.

(3) Quantitative analysis of gravity anomalies by the use of methodologies developed in magnetic prospecting for complex environments is perspective and its evaluation will be helpful.

(4) Apparently, very precise gravity gradiometry (surface and airborne) may be employed for detecting various small targets in subsurface or recognizing some thin peculiarities of geological, environmental and artificial objects.

(5) An important key way of the regional gravity data examination is increasing accuracy of satellite gravity analysis and simultaneously decreasing the distance between the grid points.

(6) Investigation of the Moon-Sun gravity influence to the Earth's environment must be continued.

(7) Increasing of the space positioning accuracy may trigger an extensive application of the ROV gravity low-altitude observations.

References

[1] Clegg, B., 2017. Gravity: How the Weakest Force in the Universe Shaped Our Lives. St. Martin's Press, N.Y.

[2] Aleinikov, A.L., Belikov, V.T. and Eppelbaum, L.V., 2001. *Some Physical Foundations of Geodynamics*. Kedem Printing-House, Tel Aviv, Israel (in Russian, contents and summary in English).

[3] Andersen, O.B., Knudsen, P. and Berry, P.A.M., 2009. The DNSC-08GRA global marine gravity field from double retracked satellite altimetry. *Journal of Geodesy*, **84**, No. 3, 191-199.

[4] Sandwell, D.T., Garcia, E., Soofi, K., Wessel, P. and Smith, W.H.F., 2013. Toward 1 mGal global marine gravity from CryoSat-2, Envisat, and Jason-1. *The Leading Edge*, **32**, No. 8, 892-899.

[5] Flechtner, F., Sneeuw, N. and Schub, W.-D., 2014. *Observation of the System Earth from Space – CHAMP, GRACE, GOCE and Future Missions*. Springer, Heidelberg – N.Y.

[6] Dehlinger, P., 1978. *Marine Gravity*. Elsevier, Amsterdam.

[7] Parasnis, D.S., 1986. *Principles of Applied Geophysics*, 4th ed., rev. and suppl. Chapman & Hall, London.

[8] Veselov, K.E., 1986. *Gravity Prospecting*. Nedra, Moscow (in Russian).

[9] Dobrin, M.B. and Savit, C.H., 1988. *Introduction to Geophysical Prospecting*. McGraw-Hill, N.Y.

[10] Telford, W.M., Geldart, L.P. and Sheriff, R.E., 1990. *Applied Geophysics*. Cambridge Univ. Press, Cambridge.

[11] Khesin, B.E., Alexeyev, V.V. and Eppelbaum, L.V., 1996. *Interpretation of Geophysical Fields in Complicated Environments*. Kluwer Academic Publishers (Springer), ***Ser.: Modern Approaches in Geophysics,*** Boston – Dordrecht – London.

[12] Kaufman, A.A. and Hansen, R.O., 2008. *Principles of the Gravitational Method*. Elsevier, Amsterdam.

[13] Jacoby, W. and Peter, S., 2009. *Gravity Interpretation. Fundamentals and Application of Gravity Inversion and Geological Interpretation*. Springer, Dordrecht – Berlin.

[14] Johannes, W.J. and Smilde, P.L., 2009. *Gravity Interpretation – Fundamentals and Application of Gravity Inversion and Geological Interpretation*. Springer, Berlin – Heidelberg.

[15] Gupta, H.K., 2011. *Encyclopedia of Solid Earth Geophysics*. Springer, Dordrecht.

[16] Eppelbaum, L.V., 2011. Review of environmental and geological microgravity applications and feasibility of their implementation at archaeological sites in Israel. *International Journal of Geophysics*, doi: 10.1155/2011/927080, ID 927080, 1-9.

[17] Eppelbaum, L.V. and Khesin, B.E., 2012. *Geophysical Studies in the Caucasus*. Springer, Heidelberg – N.Y. – London.

[18] Eppelbaum, L.V. and Khesin, B.E., 2004. Advanced 3-D modelling of gravity field unmasks reserves of a pyrite-polymetallic deposit: A case study from the Greater Caucasus. *First Break*, **22**, No. 11, 53-56.

[19] Eppelbaum, L.V., Khesin, B.E. and Itkis, S.E., 2001. Prompt magnetic investigations of archaeological remains in areas of infrastructure development: Israeli experience. *Archaeological Prospection*, **8**, No. 3, 163-185.

[20] Eppelbaum, L.V. and Mishne, A.R., 2011. Unmanned Airborne Magnetic and VLF investigations: Effective Geophysical Methodology of the Near Future. *Positioning*, **2**, No. 3, 112-133.

[21] Butler, D. K., 1984. Microgravimetric and gravity-gradient techniques for detection of subsurface cavities. *Geophysics*, **49**, No. 7, 1084-1096.

[22] Rybakov, M., Goldshmidt, V., Fleischer, L. and Rotstein, Y., 2001. Cave detection and 4-d monitoring: a microgravity case history near the Dead Sea. *The Leading Edge,* **20**, No. 8, 896-900.

[23] Debeglia, N., Bitri, A. and Thierry, P., 2006. Karst investigations using microgravity and MASW; Application to Orléans, France. *Near Surface Geophysics*, **4**, 215-225.

[24] Eppelbaum, L.V., Ezersky, M.G., Al-Zoubi, A.S., Goldshmidt, V.I. and Legchenko, A., 2008. Study of the factors affecting the karst volume assessment in the Dead Sea sinkhole problem using microgravity field analysis and 3D modeling. *Advances in GeoSciences*, **19**, 97-115.

[25] Leucci, J. and de Giorgi, L., 2010. Microgravimetric and ground penetrating radar geophysical methods to map the shallow karstic cavities network in a coastal area (Marina Di Capilungo, Lecce, Italy). *Exploration Geophysics*, **41**, 178-188.

[26] Al-Zoubi, A., Eppelbaum, L., Abueladas, A., Ezersky, M. and Akkawi, E., 2013. Methods for removing regional trends in microgravity under complex environments: testing on 3D model examples and investigation in the Dead Sea coast. *International Journal of Geophysics*, Vol. **2013**, Article ID 341797, 1-13, http://dx.doi.org/10.1155/2013/341797.

[27] Zhou W., Li, J. and Du, X., 2014. Semiautomatic interpretation of microgravity data from subsurface cavities using curvature gradient tensor matrix. *Near Surface Geophysics,* **12**, 579-586.

[28] Glosson, D. and Karaki, N.A., 2009. Salt karst and tectonics: sinkholes development along tension cracks between parallel strike-slip faults, Dead Sea, Jordan. *Earth Surface Processes and Landforms*, **34**, 1408-1421.

[29] Deroussi, S, Diament, M., Feret, J.B., Nebut, T. and Staudacher, Th., 2009. Localization of cavities in a thick lava flow by microgravimetry. *Journal of Volcanology and Geothermal Research*, **184**,193-198.

[30] Rosas-Carbajal, M., Jourde, K., Marteau, J., Deroussi, S., Komorowski, J.-C., and Gibert, D., 2017. Three-dimensional density structure of La Soufrère de Guadeloupe lava dome from simultaneous muon radiographies and gravity data. *Geophysical Research Letters*, 1-9, 0.1002/2017GL074285.

[31] Elawadi, E., Salem, A. and Ushijima, K., 2001. Detection of cavities and tunnels from gravity data using a neural network. *Exploration Geophysics*, **32**, 204-208.

[32] Wilson, S.S., Crawford, N.C., Croft, L.A., Howard, M., Miller, S., Rippy, T., 2006. Autonomous Robot for Detecting Subsurface Voids and Tunnels using Microgravity. *Proc. of SPIE*, **Vol**. 6201, 620111-1, 1-9, doi: 10.1117/12.665030.

[33] Blecha, V. and Mašin, D., 2013. Observed and calculated gravity anomalies above a tunnel driven in clays – implication for errors in gravity interpretation. *Near Surface Geophysics,* **11**, 569-578.

[34] Eppelbaum, L.V., 2013. Non-stochastic long-term prediction model for US tornado level. *Natural Hazards*, **69**, No. 3, 2269-2278.

[35] Eppelbaum, L. and Isakov, A., 2015. Implementation of the geo-correlation methodology for predictability of catastrophic weather events: long-term US tornado season and short-term hurricanes. *Environmental Earth Sciences*, **74**, 3371-3383.

[36] Lakshmanan, J. and Montlucon, J., 1987. Microgravity probes the Great Pyramide. *The Leading Edge*, No. 1, 10-17.

[37] Linford, N.T., 1998. Geophysical survey at Boden Vean, Cornwall, including an assessment of the microgravity technique for the location of suspected archaeological void features. *Archaeometry,* **40**, No. 1, 187-216.

[38] Slepak, Z., 1999. Electromagnetic sounding and high precision gravimeter survey define ancient stone building remains in the territory of Kazan Kremlin (Kazan, Republic of Tatarstan, Russia). *Archaeological Prospection*, **6**, 147-160.

[39] Di Filippo, M., Santoro, S. and Toro, B., 2005. Microgravity survey of Roman Amphitheatre of Durres (Albania). *Trans. of 6th Archaeological Prospection*, Rome (Italy), 1-4.

[40] Abad, Ir.R., García, F.G., Abad, Is.R., Blanco, M.R., Conesa, J.L.M., Marco, J.B. and Lladro, R.C., 2007. Non-destructive assessment of a buried rainwater cistern at the Carthusian Monastery 'Vall de Crist' (Spain, 14th century) derived by microgravimetric 2D modeling. *Journal of Cultural Heritage*, **8**, 197-201.

[41] Castiello, G., Florio, G., Grimaldi, M. and Fedi, M., 2010. Enhanced methods for interpreting microgravity anomalies in urban areas. *First Break*, **28**, No. 8, 93-98.

[42] Eppelbaum, L.V., 2010. Archaeological geophysics in Israel: Past, Present and Future. *Advances in Geosciences*, **24**, 45-68.

[43] Eppelbaum, L.V., 2013b. Potential geophysical fields – inexpensive effective interpretation tool at archaeological sites in the Near East. *Izv. Acad. Sci. Azerb. Rep., Ser.: Earth Sciences*, No. 3, 23-42.

[44] Padin, J., Martin, A. and Anquela, A.B., 2012. Archaeological microgravimetric prospection inside don church (Valencia, Spain). *Archaeological Prospection*, **39**, 547-554.

[45] van Gelderen, M., Haagmans, R. and Bilker, M., 1999. Gravity changes and natural gas extraction in Groningen. *Geophysical Prospecting*, **47**, 979-993.

[46] Bate, D., 2005. 4D reservoir volumetrics: A case study over the Izaute gas storage facility. *First Break*, **23**, Mo. 11, 69-71.

[47] Eiken, O., Stenvold, T., Zumberge, M., Alnes, H. and Sasagawa, G., 2008. Gravimetric monitoring of gas production from the Troll field. *Geophysics*, **73**, No. 6, WA149–WA154.

[48] Ferguson, J.F., Chen, T., Brady, J., Aiken, C.L.V. and Seibert, J., 2007. The 4D microgravity method for waterflood surveillance II — Gravity measurements for the Prudhoe Bay reservoir, Alaska. *Geophysics*, **72**, No. 2, I33-I43.

[49] Kazama, T. and Okubo, S., 2009. Hydrological modeling of groundwater disturbances to observed gravity: Theory and application to Asama Volcano, Central Japan. *Journal of Geophysical Research*, **114**, 1-11, B08402.

[50] Creutzfeldt, B., Güntner, A., Wziontek, H. and Merz, B., 2010. Reducing local hydrology from high-precision gravity measurements: a lysimeter-based approach. *Geophysical Journal International*, **183**, 178-187.

[51] Eppelbaum, L., Yakubov, Ya. and Ezersky, M., 2010. Method for comprehensive computing of water flows geodynamics in the Dead Sea basin. *Trans. of the XXXV EGS Meet.*, Zurich, Switzerland, P24, 1-4.

[52] Rymer, H., 2016. Gravity measurements on chips. *Nature*, **531**, 585-586.

[53] Imanishi, Y., Sato, T., Higashi, T., Sun, W. and Okubo, S., 2004. A network of superconducting gravimeters detects submicrogal coseismic gravity changes. *Science*, **306** (5695), 476-478, doi: 10.1126/science.1101875.

[54] Dobrovolsky, I.P., 2005. Gravity precursors of the tectonics earthquake. *Physics of the Earth*, *Izv. Russ. Acad. Sci*., **4**, 23-28.

[55] Cambiotti, G. and Sabadini, R., 2013. Gravitational seismology retrieving Centroid-Moment-Tensor solution of the 2011 Tohoku earthquake. *Jour. of Geophysical Research*, **118**, 1-12, doi: 10.1029/2012JB009555.

[56] Chen, S., Jiang, C.S. and Zhuang J.C., 2015. Statistical evaluation of efficiency and possibility of earthquake predictions with gravity field variations and its analytic signal in western China. *Pure & Appl. Geophys*., 1-15, doi: 10.1007/s00024-015-1114-x.

[57] Telesca, L., Lovallo, M., Mammadov, S., Kadirov, F. and Babayev, G., 2015. Power spectrum analysis and multifractal detrended fluctuation analysis of Earth's gravity time series. *Physica A: Statistical Mechanics and its Applications*, **248**, 426-434.

[58] Sobisevich, A.L., Sobisevich, L.E., Kanonidi, K.H. and Likhodeyev, D.B., 2017. On the gravity-magnetic disturbances preceding the seismic events. *Doklady Russ. Acad. Sci*., **475**, No. 4, 444-447.

[59] Battaglia, M., Gottsman, J., Carbone, D. and Fernandez, J., 2008. 4D volcano gravimetry. *Geophysics*, **73**, No.6, WA3-WA18.

[60] Rymer, H., Locke, S.A., Borgia, A., Martinez, M., Brenes, J., Van der Laat, R. and Williams-Jone, G., 2009. Long-term fluctuations in volcanic activity: implications for future environmental impact. *Terra Nova*, **21**, No. 4, 304–309.

[61] Greco, F., Currenti, G., Del Negro, C., Napoli, R., Budetta, G., Fedi, M. and Boschi, E., 2010. Spatiotemporal gravity variations to look deep into the southern flank of Etna volcano. *Journal of Geophysical Research*, **115**, B11411, doi: 10.1029/2009JB006835.

[62] Aparicio, S.S.-M., Sampedro, J.A., Montesinos, F.G. and Molist, J.M., 2011. Volcanic signatures in time gravity variations during the volcanic unrest on El Hierro (Canary Islands). *Journal of Geophysical Research*: *Solid Earth*, 5033-5051, doi: 10.1002/2013JB010795.

[63] Zurek, J., William-Jones, G., Johnson, D. and Eggers, A., 2012. Constraining volcanic inflation at Three Sisters Volcanic Field in Oregon, USA, through microgravity and deformation modeling. *Geochemistry, Geophysics, Geosystems*, **3**, No. 10, 1-15, doi: 10.1029/2012GC004341.

[64] Alizadeh, A. A., Guliyev, I. S., Kadirov, F. A. and Eppelbaum, L. V., 2016. *Geosciences of Azerbaijan*. Volumes I & II. Springer, Heidelberg – N.Y. – London.

[65] Poltoratsky, V.V. and Ginzburg, S.N., 1989. Gravity prospecting. *In*: (Brodovoi, V.V., Ed.) *Borehole and Mining Geophysics*, Vol II. Nedra, Moscow, 190-209 (in Russian).

[66] Madej, J., 2017. Gravimetric surveys for assessing rock mass condition around a mine shaft. *Acta Geophysica*, **65**, 465-479.

[67] Nettleton, L.L., 1976. *Gravity and Magnetics in Oil Prospecting*. McGraw-Hill, N.Y.

[68] Berezkin, V.M., 1988. *Total Gradient Method in Geophysical Prospecting*. Nedra, Moscow (in Russian).

[69] Tzimelzon, I.O., 1965. Earth's crust deep structure and tectonics of Azerbaijan by geophysical data. *Soviet Geology*, No. 4, 103-111 (in Russian).

[70] Gadirov, V.G. and Eppelbaum, L.V., 2012. Detailed gravity, magnetics successful in exploring Azerbaijan onshore areas. *Oil and Gas Journal,* **110,** No. 11, 60-73.

[71] Leonov, Yu.G. (Ed.), 2008. *The Greater Caucasus in the Alpine Epoch*. Geos, Moscow (in Russian).

[72] Eppelbaum, L.V., 2015. Comparison of 3D integrated geophysical modeling in the South Caucasian and Eastern Mediterranean segments of the Alpine-Himalayan tectonic belt. *Izv. Acad. Sci. Azerb. Rep., Ser.: Earth Sciences*, No. 3, 25-45.

[73] Khain, V.E., 2001. *Tectonics of Continents and Oceans*. Scientific World, Moscow (in Russian).

[74] Eppelbaum, L. and Khesin, B., 2011. Development of 3-D gravity-magnetic models of Earth's crust of Azerbaijan and adjacent areas: A generalized review. *Positioning*, **2**, No. 2, 84-102.

[75] Pavlenkova, G.A., 2012. Structure of the Caucasus' earth crust along the deep seismic sounding profiles Stepnoe-Bakuriani and Volgograd-Nakhchevan (results of initial data re-interpretation). *Izvestiya*, *Physics of the Earth*, No. 5, 16-25.

[76] Pilchin, A.N. and Eppelbaum, L.V., 1997. Determination of magnetized bodies lower edges by using geothermal data. *Geophysical Journal International*, **128**, No. 1, 167-174.

[77] Ben-Avraham, Z., Ginzburg, A., Makris, J. and Eppelbaum, L., 2002. Crustal structure of the Levant basin, Eastern Mediterranean. *Tectonophysics*, **346**, 23-43.

[78] Rotstein, Y. and Bartov, Y. 1989. Seismic reflection across a continental transform: An example from a convergent segment of the Dead Sea rift. *Jour. of Geophys*. *Research*, **94**, 2902-2912.

[79] Rotstein, Y., Bartov, Y., Freislander, U. 1992. Evidence for local shifting of the main fault and changes in the structural setting, Kinarot basin, Dead Sea transform. *Geology*, **20**, 251-254.

[80] Ben-Avraham, Z., Ten-Brink, U., Bell, R. and Reznikov, M., 1996. Gravity field over the Sea of Galilee: evidence for a composite basin along a transform fault. *Jour. Geophys. Research*, **101**, 533-544.

[81] Eppelbaum, L. V. and Pilchin, A. N., 2006. Methodology of Curie discontinuity map development for regions with low thermal characteristics: An example from Israel. *Earth and Planetary Sciences Letters*, **243**, No. 3-4, 536-551.

[82] Eppelbaum, L.V., Ben-Avraham, Z. and Katz, Y.I., 2007. Structure of the Sea of Galilee and Kinarot Valley derived from combined geological-geophysical analysis. *First Break*, **25**, No. 1, 21-28.

[83] Meiler, M., Reshef, M. and Shulman, H. 2011. Seismic depth-domain stratigraphic classification of the Golan Heights, central Dead Sea Fault. *Tectonophysics*, **510**, 354-369.

[84] Ben-Avraham, Z., Rozenthal, M., Tibor, G., Navon, H., Wust-Bloch, H., Hofstetter, R., Rybakov, M., 2014. In: Structure and Tectonic Development of the Kinneret Basin (Ed. T. Zohary et al.) *Lake Kinneret, Ecology and Management*, Aquatic Ecology Series **6**, Springer, 19-38.

[85] Stern, R. J., Johnson, P. R., Kroner, A. and Yibas, B., 2004. Neoproterozoic ophiolites of the Arabian-Nubian Shield. *Developments in Precambrian Geology*, **13**, 95-128.

[86] Johnson, P.R. and Kattan, F.H., 2008. Lithostratigraphic revision in the Arabian shield: The impacts of geochronology and tectonic analysis. *The Arabian Jour. for Science and Engin*., **33**, No. 1, 3-16.

[87] Gurevich, E.L., 1981. Paleomagnetism of Upper Precambrian rocks of Irkutian amphitheatre; Problems of their correlation and paleogeographic location. In: *Paleomagnetism and Problems of Paleogeography*, *Transactions of VNIGRI*, 11-22 (in Russian).

[88] Molostovsky, E.A., Molostovsky, I.I. and Minikh, M.G. 1998. Stratigraphic correlations of the Upper Permian and Triassic beds from the Volga-Ural and Cis-Caspian. In: (Crasquin-Soleau, S. and Barrier, E´., Eds.) *Peri-Tethys memoir 3: Stratigraphy and Evolution of Peri-Tethyan platforms*. Me´moires du Muse´um national d'histoire naturelle, Paris, **177**, 35-44.

[89] Ben-Avraham, Z., 1978. The structure and tectonic setting of the Levant continental margin, Eastern Mediterranean. *Tectonophysics*, **46**, 313-331.

[90] Robertson, A. H. F. and Dixon, J.E., 1984. Introduction: aspects of the geological evolution of the Eastern Mediterranean. *In*: (Dixon J.E., Robertson A.H.F., Eds.), *The Geological Evolution of the Eastern Mediterranean*, Geological Society Special Publ. No. 17, 1-74.

[91] Ben-Avraham, Z. and Ginzburg, A., 1990. Displaced terranes and crustal evolution of the Levant and the eastern Mediterranean. *Tectonics*, **9**, 613-622.

[92] Hall, J. K., Krasheninnikov, V. A., Hirsch, F., Benjamini, C. and Flexer, A. (Eds.), 2005. *Geological framework of the Levant*, Volume II: The Levantine Basin and Israel, Jerusalem.

[93] Krasheninnikov, V. A., Hall, J. K., F. Hirsch, H. Benjamini, and A. Flexer (Eds.), 2005. *Geological*

Framework of the Levant, Volume 1: Cyprus and Syria, Jerusalem.

[94] Ben-Avraham, Z., Schattner, U., Lazar, M., Hall, J. K., Ben-Gai, Y., Neev, D. and Reshef, M., 2006. Segmentation of the Levant continental margin, eastern Mediterranean. *Tectonics,* **25**, TC5002, 1-17.

[95] Reilinger, R. E., McClusky, S., Vernant, P., Lawrence, S., Ergintav, S., Cakmak, R., Ozener, H., Kadirov, F., Guliev, I., Stepanyan, R., Nadariya, M., Hahubia, G., Mahmoud, S., Sakr, K., ArRajehi, A., Paradissis, D., Al-Aydrus, A., Prilepin, M., Guseva, T., Evren, E., Dmitrotsa, A. Filikov, S. V., Gomez, F., Al-Ghazzi, R. and Karam, G., 2006. GPS constraints on continental deformation in the Africa-Arabia-Eurasia continental collision zone and implications for the dynamics of plate interactions. *Jour. of Geophysical Research,* BO5411, 1-26, doi: 10.1029/2005JB004051.

[96] Le Pichon, X. and Kreemer, C., 2010. The Miocene-to-present kinematic evolution of the Eastern Mediterranean and Middle East and its implications for Dynamics. *Annu. Rev. Earth Planet. Sci*., **38**, 323-351.

[97] Eppelbaum, L**.** and Katz, Y., 2011. Tectonic-Geophysical Mapping of Israel and eastern Mediterranean: Implication for Hydrocarbon Prospecting. *Positioning*, **2,** No. 1, doi: 10.4236/pos.2011.21004, 36-54.

[98] Eppelbaum, L.V. and Katz, Yu.I., 2015. Eastern Mediterranean: Combined geological-geophysical zonation and paleogeodynamics of the Mesozoic and Cenozoic structural-sedimentation stages. *Marine and Petroleum Geology*, **65**, 198-216.

[99] Eppelbaum, L.V. and Katz, Y.I., 2012. Key features of seismo-neotectonic pattern of the Eastern Mediterranean. *Izvestiya Acad. Sci. Azerb. Rep., Ser.: Earth Sciences*, No. 3, 29-40.

[100] Schenk, C.J., Kirschbaum, M.A., Charpentier, R.R., Klett, T.R., Brownfield, M.E., Pitman, J.K., Cook T.A. and Tennyson M.E., 2010. Assessment of undiscovered oil and gas resources of the Levant Basin Province, Eastern Mediterranean. *U.S. Geological Survey Fact Sheet 2010-3014*, 1-4.

[101] Eppelbaum, L.V., Katz, Y.I. and Ben-Avraham, Z., 2012. Israel – Petroleum Geology and Prospective Provinces. *AAPG European Newsletter*, No. 4, 4-9.

[102] Montadert, L., Nicolaides, S., Semb, P.H., Lie, Ø., 2014. Petroleum systems offshore Cyprus. In: (Marlow, L., Kendall, C. and Yose, L., Eds.), Petroleum Systems of the Tethyan Region, AAPG Memoir 106, 301-334.

[103] Eppelbaum, L.V. and Katz, Yu.I., 2016. Tectono-Geophysical Zonation of the Near and Middle East and Eastern Africa. *International Journal of Geology*, **10**, 1-10.

[104] Li, Y., Braitenberg, C. and Yang, Y., 2013. Interpretation of gravity data by the continuous wavelet transform: The case of the Chad lineament (North-Central Africa). *Journal of Applied Geophysics*, **90**, 62-70.

[105] Klokočník, J., Kostelecký, J., Eppelbaum, L. and Bezděk, A., 2014. Gravity disturbances, the Marussi tensor, invariants and other functions of the geopotential represented by EGM 2008. *Journal of Earth Science Research*, **2**, No. 3, 88-101.

[106] Klokočník, J., Kostelecký, J., Bezděk, A., Cílek, V. and Pešek, I., 2017. A support for the existence of paleolakes and paleorivers buried under Saharan sand by means of "gravitational signal" from EIGEN 6C4. *Arabian Journal of Geosciences*, **10**, 1-28.

[107] Sandwell, D.T. and Smith, W.H.F., 2009. Global marine gravity from retracked Geosat and ERS-1 altimetry: Ridge Segmentation versus spreading rate. *Journal of Geophysical Research*, **114**, B01411, 1-18.

[108] De Mauro, A., Greco, M. and Grimaldi, M., 2016. A formal definition of Big Data based on its essential features. *Library Review*, **65**, No. 3, 122-135.

[109] Rathore, M. M., Ahmad, A., Paul, A., Hong, W.-H. and Seo, H., 2017. Advanced computing model for geosocial media using big data analytics. *Multimed Tools Appl*., doi: 10.1007/s11042-017-4644-7, 1-21.

[110] Khain, V.E., 1984. *Regional Geodynamics*. *Alpine Mediterranean Belt*. Nedra, Moscow (in Russian).

[111] Sharkov, E., Lebedev, V., Chugaevm A., Zabarinskaya, L., Rodnikov, A., Sergeeva, N. and Safonova, I., 2015. The Caucasian-Arabian segment of the Alpine-Himalayan collisional belt: Geology, volcanism and neotectonics. *Geoscience Frontiers*, **6**, No. 4, 513-522.

[112] Eppelbaum, L.V. and Katz, Yu.I., 2017. A New Regard on the Tectonic Map of the Arabian-African Region Inferred from the Satellite Gravity Analysis. *Acta Geophysica*, doi: 10.1007/s11600-017-0057-2, 1-20.

[113] Petrov, A.V., Zinovkin, S.V., Osipenkov, D.Yu. and Yudin, D.B., 2011. Computer technology of statistical and spectrum-correlation data analysis KOSKAD 3D 2011. *Geoinformatics*, No. 4, 7-13 (in Russian).

[114] Véronnet, A., 1912. Rotation de l'Ellipsoide Hétérogène et Figure Exacte de la Terre. *J. Math. Pures et Appl*., Ser. 6, **8**, 331-463.